Physics of Fluids ARTICLE scitation.org/journal/phf

Advected phase-field method for bounded solution of the Cahn–Hilliard Navier–Stokes equations

Cite as: Phys. Fluids **33**, 053311 (2021); doi: 10.1063/5.0048614
Submitted: 24 February 2021 · Accepted: 22 April 2021 ·
Published Online: 14 May 2021

Abdolrahman Dadvand,[1,2,a)] Milad Bagheri,[3] Nima Samkhaniani,[4] Holger Marschall,[3] and Martin Wörner[5]

AFFILIATIONS

[1]Institute for Chemical Technology and Polymer Chemistry, Karlsruhe Institute of Technology (KIT), Engesser Straße 20, 76131 Karlsruhe, Germany
[2]Faculty of Mechanical Engineering, Urmia University of Technology, Urmia, Iran
[3]Computational Multiphase Flow, Technische Universität Darmstadt, Alarich-Weiss Straße 10, 64287 Darmstadt, Germany
[4]Institute of Fluid Mechanics, Karlsruhe Institute of Technology (KIT), Kaiserstraße 10, 76131 Karlsruhe, Germany
[5]Institute of Catalysis Research and Technology, Karlsruhe Institute of Technology (KIT), Engesser Straße 20, 76131 Karlsruhe, Germany

[a)]**Author to whom correspondence should be addressed:** abdolrahman.dadvand@partner.kit.edu

ABSTRACT

Phase-field methods based on the Cahn–Hilliard (CH) equation coupled to the incompressible Navier–Stokes equation are becoming increasingly popular for interface resolving numerical simulations of two-phase flows of immiscible fluids. One major limitation of this approach, however, is that the volume of each phase is not inherently preserved. This is associated with the phase-discriminating order parameter, which in the course of the simulation remains in general not within its initial physical bounds. This shortcoming relates to the fact that the CH equation with standard Ginzburg–Landau chemical potential has no volume-preserving stationary solution for interfaces with uniform (non-zero) curvature. In this paper, a curvature-dependent chemical potential is proposed which allows for bounded stationary solutions of the CH equation for drops/bubbles exhibiting uniform curvature. Numerical solutions of the coupled Cahn–Hilliard Navier–Stokes equations show that the proposed chemical potential significantly improves boundedness and phase volume conservation over the standard one.

I. INTRODUCTION

Two-phase flow problems have attracted increasing attention due to their wide-spread industrial and scientific applications. In most situations, the thickness of the interface between the two phases is so small that the sharp interface model (Leal, 2010), where the fluid flow within each phase is governed by the Navier–Stokes (NS) equations and the two phases are connected by the boundary conditions at the interface, can accurately capture the flow physics. However, as the locations of the interfaces are normally not known *a priori*, it is a cumbersome task to explicitly impose the boundary conditions at the interfaces. Methods that use an explicit representation of the interface, involving computational mesh motion and deformation, such as arbitrary Lagrangian–Eulerian (ALE) methods (Chatzidai *et al.*, 2009) or front-tracking methods (Tryggvason *et al.*, 2001), can provide an accurate representation of surface tension, but they have difficulty in dealing with complex and evolving interface topologies (Fuster *et al.*, 2009). On the other hand, methods that use an implicit representation of the interface such as marker-and-cell (MAC), volume of fluid (VOF), and level-set can robustly and efficiently represent evolving, topologically complex interfaces but generally suffer from an inaccurate representation of surface tension (Francois *et al.*, 2006).

An alternative approach to capture the topological evolution of an interface is the phase-field (or diffuse interface) method. The main idea of this approach is to implicitly describe the interface by a continuous scalar field, i.e., the phase-field, varying continuously (but rapidly) over a thin transitional layer of well-defined finite thickness and being mostly uniform in the bulk phases (Badalassi *et al.*, 2003; Yue *et al.*, 2004). In this approach, diffusion is allowed to occur between

the two fluid components through gradients of the chemical potential of the system in their thin interfacial region (Sibley *et al.*, 2013). Two widely used phase-field models are the Allen–Cahn (AC) equation (Allen and Cahn, 1979) and the Cahn–Hilliard (CH) equation (Cahn and Hilliard, 1958). Both of these two models attempt to minimize the Ginzburg–Landau (GL) free energy functional, but in two different norms (Mirjalili *et al.*, 2020).

The AC model is a second order partial differential equation (PDE) which is not readily suitable for simulation of immiscible, incompressible two-phase flows due to its non-conservative nature. This is attributed to the absence of the interface deformation/curvature contribution in the standard Helmholtz free energy functional (Wacławczyk, 2017). Many researchers have attempted to overcome this issue by introducing time-dependent Lagrange multipliers (Rubinstein and Sternberg, 1992; Yang *et al.*, 2006; and Zhang and Tang, 2007) and space and time dependent Lagrange multipliers (Brassel and Bretin, 2011; Jeong and Kim, 2017; Joshi and Jaiman, 2018; Kim *et al.*, 2014; Lee and Kim, 2020; and Zhai *et al.*, 2015) as non-local corrections to the original PDE. Besides, a few local modifications have been done to the AC equation. In their study of the Saffman–Taylor instability, Folch *et al.* (1999) introduced a so-called *counterterm*, i.e., $\kappa|\nabla c|$ (where κ is the local curvature field defined everywhere in space, which corresponds to the curvature of the isocontours of the order parameter c) to the original AC phase-field equation in order to cancel the curvature effect at the leading order. In this manner, the typical hyperbolic tangent profile is still obtained as the solution of the AC phase-field equation, but it is simply advected by the interface motion [therefore the name advected-field method (Plapp, 2012)] and not modified by curvature effects (Biben *et al.*, 2003). Sun and Beckermann (2007) proposed a second order phase-field equation derived from an interface advection equation by expressing the interface normal and curvature in terms of a hyperbolic tangent phase-field profile across the interface. They also considered the interface motion due to an arbitrary external velocity field. In the absence of curvature-driven interface motion, the so-called counterterm introduced by Folch *et al.* (1999) is used in the equation to cancel out such motion. A conservative form of the formula proposed by Sun and Beckermann (2007) was obtained by Chiu and Lin (2011). This conservative second order phase-field equation has been widely used in the numerical simulation of two-phase flows (Chai *et al.*, 2018; Geier *et al.*, 2015; Hu *et al.*, 2018; 2019; and Liang *et al.*, 2018). In addition, a Lagrange multiplier combining both local and non-local effects is rigorously investigated in Alfaro and Alifrangis (2014).

The CH model is a fourth-order PDE, which is becoming more popular in simulating two-phase flows due to its conservative properties and robustness (Jacqmin, 1999; Li *et al.*, 2020; Liu *et al.*, 2019; Ma *et al.*, 2020; Niu *et al.*, 2018; and Zanella *et al.*, 2020). As a distinct advantage, the CH equation ensures the conservation of "total mass," interpreted as the volume integral of c in the computational domain. If the order parameter is strictly bounded so that the values in the bulk of each component are ± 1 and if the interface of the two phases is a hyperbolic tangent profile (equilibrium state), then the mass of each component is conserved as well (Li *et al.*, 2016). However, if the order parameter is not bounded so that its values in the bulk regions deviate from ± 1 [due to the so-called bulk diffusion resulting from adoption of a double-well potential in CH equation (Soligo *et al.*, 2019)], shrinkage/expansion occurs and the volume of the phase enclosed by the interface diffuses into the other phase to restore the equilibrium profile (Yue *et al.*, 2007). This way the "total mass" is still conserved, but there is a mass leakage among the two phases that can affect the computational accuracy of the interface position and surface tension force (Li *et al.*, 2016).

Thus far, three main strategies have been applied to overcome the limitations of the original CH equation concerning boundedness and phase mass conservation: (i) using degenerate mobility instead of non-degenerate (constant) mobility (Ceniceros and García-Cervera, 2013; Dai and Du, 2016; Elliott and Garcke, 1996; Liu, 2008; Kim and Kang, 2009; Lee *et al.*, 2016; Lee and Kim, 2016; and Shah *et al.*, 2019), (ii) introducing correction terms into the CH equation (Li *et al.*, 2016), and (iii) increasing local or global grid resolution (Ding and Yuan, 2014). Degenerate mobility function guarantees that the order parameter maintains within the physical bound $c \in [-1, +1]$ (Boyer, 1999; Abels *et al.*, 2013), though the bounded solutions are not always compatible with the physical features of the problem, such as the Gibbs–Thomson effect (Dai and Du, 2016). Introducing an interfacial correction term into the CH equation as proposed by Li *et al.* (2016) can improve the accuracy of the original model. Wang *et al.* (2018) presented an improved CH model with a re-initialization process for capturing the interface more accurately. Their method was able to reduce numerical diffusion effectively and obtain a fluid interface that is physically close to its equilibrium state. The grid resolution methods are able to improve the interface sharpness but they do not guarantee the interface profile in the equilibrium state.

An important contribution to obtain solutions of the CH equation which conserve mass of each phase and are albeit physically sound is given by the relation between density and order parameter. As in the absence of special measures the CH equation may yield unbounded solutions, linear relations $\rho(c)$ might lead to nonphysical negative densities, especially if the density ratio is large (Kim, 2012). Bonart *et al.* (2019b) used a thermodynamically consistent CH model with a nonlinear relation between density and order parameter. They found that unlike the linear relations, the non-linear relation enforces positive densities. However, it can lead to loss of total mass during the simulations (Bonart *et al.*, 2019a; 2019b).

From the above discussion, it is clear that obtaining bounded and potentially stationary solutions of the order parameter is of utmost importance to ensure mass conservation of the individual phases in the CH equation. As the curvature driven motion in the presence of curved interfaces is inherent in currently used chemical potentials, no such stationary solutions of the CH equation are possible. Stationary phase distributions of single drops or bubbles are only possible when the CH equation is coupled with the incompressible NS equations, where mass/volume conservation is ensured by the condition of a divergence-free velocity field. In the present work, the original CH equation is modified by introducing a curvature-dependent chemical potential. As we shall see, the proposed chemical potential allows for a stationary solution of the CH equation for bubbles or droplets with uniform (non-zero) curvature. Hence, it guarantees bounded solutions for two-phase flow problems with both planar and non-planar interfaces. The effectiveness of this advected-field chemical potential is justified by applying it to several benchmark two-phase flow problems.

II. GOVERNING EQUATIONS AND NUMERICAL METHOD

This section is devoted to the governing equations, i.e., the Cahn–Hilliard and the Navier–Stokes equations within a diffuse

interface modeling framework. First, a curvature-dependent chemical potential allowing for stationary solution of the CH equation is derived and a modified interfacial energy density for capillary interfaces is proposed. This is followed by the numerical solution approach, where a special treatment for calculation of the interface unit normal vector needed for curvature computation is introduced.

A. Cahn–Hilliard equation with advected-field chemical potential

1. General considerations

Consider a system of two immiscible fluids in contact with each other. The composition order parameter $c \in [-1, +1]$ is defined as the phase-field parameter such that in the two fluid bulks $c = \pm 1$, and the fluid–fluid interface is given by $c = 0$. Denoting the fluid domain by Ω, the Helmholtz free energy functional is written as

$$\mathcal{F}[c] = \int_\Omega \lambda \left\{ \frac{\psi(c)}{\varepsilon^2} + \frac{1}{2}[\nabla c]^2 \right\} \mathrm{d}\Omega, \tag{1}$$

where $\psi(c)$ is a double-well potential that describes the bulk coexistence of the two phases and the second term $[\nabla c]^2/2$ is the gradient contribution. A simple prescription for $\psi(c)$ is the Ginzburg–Landau double-well potential, $\psi(c) = (1 - c^2)^2/4$, which determines the values of the coexisting bulk phases as ± 1. In addition, λ is the mixing energy density and ε is the capillary width of the diffuse interface.

A variational procedure (Cahn and Hilliard, 1958) leads to the generalized chemical potential ϕ as

$$\phi(c) = \frac{\delta \mathcal{F}[c]}{\delta c} = \frac{\partial \mathcal{F}[c]}{\partial c} - \nabla \cdot \left[\frac{\partial \mathcal{F}[c]}{\partial (\nabla c)} \right] = \lambda \left(\frac{1}{\varepsilon^2} \psi'(c) - \nabla^2 c \right), \tag{2}$$

where $\psi'(c) = \mathrm{d}\psi/\mathrm{d}c = c^3 - c$. The CH equation is written as

$$\frac{\partial c}{\partial t} + \nabla \cdot (c\,\mathbf{u}) = -\frac{2}{\rho^+ - \rho^-} (\nabla \cdot \mathbf{J}), \tag{3}$$

where $\mathbf{u}$ is the divergence-free velocity field and $\mathbf{J}$ denotes the phase-field diffusion flux defined as $\mathbf{J} = -0.5(\rho^+ - \rho^-) M \nabla \phi$ (Yue, 2020; Zhu *et al.*, 2019). Here, ρ is the density, the superscripts $+$ and $-$ denote the bulk values, and M is the mobility coefficient between the phases $+$ and $-$. The terms on the left-hand side of Eq. (3) express the hydrodynamic transport of the phase-field by the flow while the term on the right-hand side is responsible for the diffusive relaxation of the field to its equilibrium state.

The non-negative mobility coefficient M is considered often as either a constant or a concentration-dependent variable (Khatavkar *et al.*, 2007; Shah *et al.*, 2019). Generally, it is desirable to keep M small such that the interface position is primarily advected. At the same time, it requires to be big enough to ensure that the interface profile is accurately modeled and the interface thickness remains approximately constant (Aland, 2012). Asymptotic analysis (Abels *et al.*, 2012) and numerical benchmarks (Aland, 2012) demonstrate that this can be achieved by taking the scaling $M \sim \varepsilon^2$. For a constant mobility coefficient ($M = \text{const.}$), Eq. (3) becomes

$$\frac{\partial c}{\partial t} + \nabla \cdot (c\,\mathbf{u}) = M \nabla^2 \phi. \tag{4}$$

Integrating Eq. (4) over the entire computational domain Ω and using the boundary conditions $(\mathbf{n} \cdot \mathbf{u})|_{\partial\Omega} = 0$ and $(\mathbf{n} \cdot \nabla\phi)|_{\partial\Omega} = 0$ (where $\partial\Omega$ denotes the boundary of the computational domain and $\mathbf{n}$ is the outward unit normal to $\partial\Omega$) yield (Yue *et al.*, 2007)

$$\frac{\mathrm{d}}{\mathrm{d}t} \int_\Omega c \,\mathrm{d}\Omega = 0, \tag{5}$$

meaning that CH dynamics conserves phase volume (total mass) over the entire domain.

In the equilibrium state without any flow ($\mathbf{u} = 0$), the spatial distribution of c is determined by the condition that the chemical potential ϕ is constant, i.e.,

$$\phi = \lambda \left(\frac{1}{\varepsilon^2} \psi'(c) - \nabla^2 c \right) = const. \tag{6}$$

For the sake of simplicity, we take $const. = 0$. Since $\lambda > 0$, Eq. (6) becomes

$$\frac{1}{\varepsilon^2} \psi'(c) - \nabla^2 c = 0. \tag{7}$$

For the reason of further exploitation, we now consider the problem in Cartesian, polar, and spherical coordinates where the order parameter varies in the direction normal to the interface, r, only, i.e., $c = c(r)$. Equation (7) can then be written in the general form as

$$\frac{1}{\varepsilon^2} \underbrace{\psi'(c)}_{=c^3 - c} - \left(\frac{\partial^2 c}{\partial r^2} + \underbrace{\frac{N-1}{r}}_{=\kappa} \frac{\partial c}{\partial r} \right) = 0. \tag{8}$$

The integer $N \in \{1, 2, 3\}$ denotes the space dimensions of the problem. In addition, the term $(N-1)/r = \kappa$ is the local curvature field defined everywhere in space, which corresponds to the curvature of the isocontours of the order parameter c.

2. Planar interface

For a planar interface ($\kappa = 0$), Eq. (8) reduces to

$$\frac{c^3 - c}{\varepsilon^2} - \frac{\partial^2 c}{\partial r^2} = 0. \tag{9}$$

The solution of Eq. (9) is the well-known hyperbolic tangent profile, $c = \tanh\left(r/\left(\sqrt{2}\,\varepsilon\right)\right)$. The interfacial tension σ for a planar interface can be derived from the CH free energy for the interface formed between $c^+ = 1$ and $c^- = -1$ as (Jacqmin, 1999)

$$\sigma = \lambda \int_{-\infty}^{\infty} \left(\frac{\partial c}{\partial r} \right)^2 \mathrm{d}r. \tag{10}$$

With the above solution of Eq. (9), the integration in Eq. (10) yields the following relation between interfacial tension, mixing energy density coefficient, and the capillary width of the diffuse interface:

$$\sigma = \frac{2\sqrt{2}\,\lambda}{3\,\varepsilon}. \tag{11}$$

3. Non-planar (curved) interfaces

It can be easily shown that for a non-planar interface ($N > 1$, $\kappa \neq 0$), the hyperbolic tangent profile is no longer the solution of Eq. (8). To maintain the hyperbolic tangent profile for non-planar interfaces, a term η serving as Lagrange multiplier needs to be added to

Eq. (8). As shown in the Appendix, a constant Lagrange multiplier η is unsuitable for this purpose. This has also been pointed out by Niethammer (1995). However, adopting

$$\eta = \frac{N-1}{r}\frac{\partial c}{\partial r} = \kappa \frac{\partial c}{\partial r} \tag{12}$$

can enforce the solution in the form of hyperbolic tangent profile. As the interface curvature depends on space (and for dynamic cases also on time), the same holds for the Lagrange multiplier η. For an equilibrium hyperbolic tangent profile, it is $\partial c/\partial r = (1-c^2)/(\sqrt{2}\,\varepsilon)$ or equivalently $\partial c/\partial r = |\nabla c|$. Therefore, in equilibrium,

$$\eta = \kappa|\nabla c|. \tag{13}$$

If c follows the hyperbolic tangent profile, η is finite in the diffuse interface region but approaches zero far from the interface. Adding η to the left-hand side of Eq. (8) cancels out the third term causing the curvature-driven interface motion which hinders the establishment of steady equilibrium states in two-phase problems with curved interfaces. In this way, the Laplacian operator in chemical potential [Eq. (6)] is effectively reduced to $\nabla^2 c + \kappa|\nabla c| \simeq \partial^2 c/\partial r^2$. This resolves the shrinkage/expansion issue occurring in two-phase flow problems (Yue *et al.*, 2007) and enforces the order parameter to be bounded within ± 1 in the bulk fluids. While obtained from a different concept as presented above, the Lagrange multiplier η in Eq. (13) takes the same form as the *counterterm* added by Folch *et al.* (1999) to the AC equation to cancel out the local Allen–Cahn dynamics of the interface. We, therefore, reformulate Eq. (7) by adding η from Eq. (13) as follows:

$$\frac{1}{\varepsilon^2}\psi'(c) - \nabla^2 c + \underbrace{\kappa|\nabla c|}_{\eta} = 0. \tag{14}$$

For bubbles and droplets with uniform interface curvature, the lower integration limit in Eq. (10) should be changed to the bubble/drop center so that

$$\sigma = \lambda \int_0^\infty \left(\frac{\partial c}{\partial r}\right)^2 \mathrm{d}r. \tag{15}$$

As the solution to Eq. (14) is $c = \tanh((r-r_0)/(\sqrt{2}\,\varepsilon))$, where r_0 is the position of the interface (determined by $c = 0$, see Fig. 1), the integration of Eq. (15) gives

$$\sigma = \frac{2\sqrt{2}\,\lambda}{3\,\varepsilon} g(Cn), \tag{16}$$

where

$$g(Cn) = \frac{e^{\frac{2}{\sqrt{2}Cn}}\left(3 + e^{\frac{1}{\sqrt{2}Cn}}\right)}{\left(1 + e^{\frac{1}{\sqrt{2}Cn}}\right)^3}. \tag{17}$$

In Eq. (17), Cn is the Cahn number defined as $Cn = \varepsilon/(2\,r_0)$. While Eq. (16) differs from that obtained for the planar interface [Eq. (11)], the difference is small provided Cn is small. In the sharp interface limit ($Cn \to 0$), $\lim_{Cn\to 0} g(Cn) = 1$ so that the value of the planar interface is approached.

4. Thermodynamic consistency

Equation (14) may be interpreted as a modified chemical potential

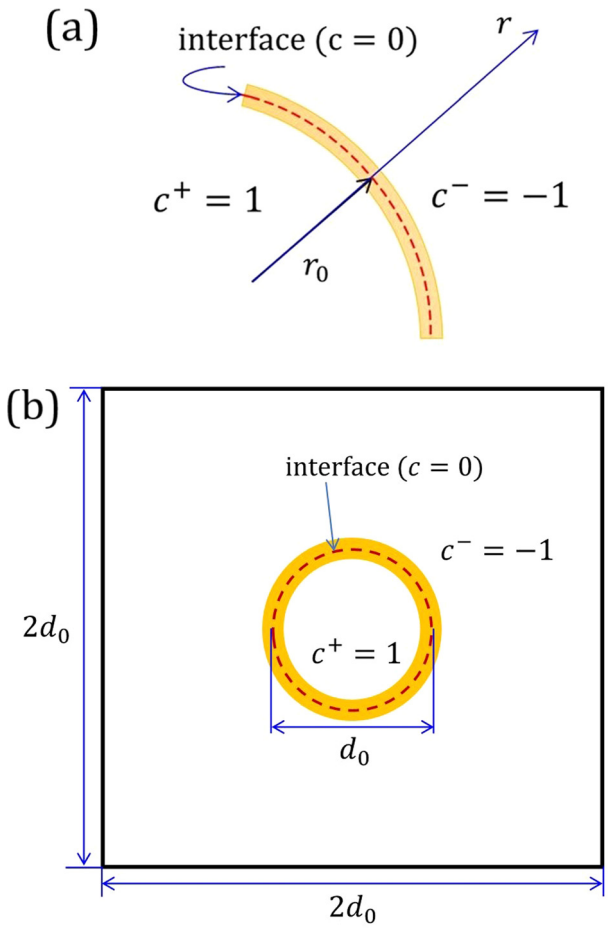

FIG. 1. Schematic representation of 1D (a) and 2D (b) stagnant two-phase problems.

$$\phi_m = \lambda\left(\frac{1}{\varepsilon^2}\psi'(c) + \kappa|\nabla c| - \nabla^2 c\right). \tag{18}$$

The wide success of phase-field models is based on energy functionals which ensure thermodynamic consistency, meaning that the total free energy, cf. Equation (1), does not increase in time. However, the chemical potential ϕ_m in Eq. (18) makes the CH equation to be thermodynamically inconsistent, i.e., no energy functional can be found to be associated with this chemical potential. To enforce thermodynamic consistency of the AC equation, Jamet and Misbah (2008) proposed replacing $|\nabla c|$ in the *counterterm* $\kappa|\nabla c|$ added by Folch *et al.* (1999) with its equivalence at equilibrium. Following Jamet and Misbah (2008), we set $|\nabla c| \simeq \sqrt{2\psi(c)}/\varepsilon$ in Eq. (18) to obtain a thermodynamically consistent phase-field model. Therefore, the advected-field chemical potential

$$\phi_{af} = \lambda\left(\frac{1}{\varepsilon^2}\psi'(c) + \frac{\sqrt{2\psi(c)}}{\varepsilon}\kappa - \nabla^2 c\right) \tag{19}$$

and the associated energy functional

$$\mathcal{F}_{\mathrm{af}}[c] = \int_{\Omega} \lambda \left\{ \frac{\psi(c)}{\varepsilon^2} - \frac{\sqrt{2\psi(c)}}{\varepsilon} |\nabla c| + \frac{1}{2} [\nabla c]^2 \right\} \mathrm{d}\Omega \tag{20}$$

are introduced.

The advected-field chemical potential ϕ_{af} given by Eq. (19) is identical as the one developed by Jamet and Misbah (2008) for the AC equation. However, to the best of our knowledge, it has not thus far been employed in any numerical simulation of two-phase flows and has remained in theoretical level. Although ϕ_{af} can be used with both the AC and CH phase-field based equations, in the present work, it is used with the CH equation. Consequently, the advected-field Cahn–Hilliard equation becomes

$$\frac{\partial c}{\partial t} + \nabla \cdot (c\,\mathbf{u}) = M \nabla^2 \phi_{\mathrm{af}}. \tag{21}$$

The Cahn–Hilliard Eq. (21) in combination with the proposed chemical potential ϕ_{af} given by Eq. (19) constitutes a thermodynamically consistent diffuse interface model. Interface curvature in Eq. (19) is computed as $\kappa = \nabla \cdot \mathbf{n}_s$ with $\mathbf{n}_s(c)$ being the outward unit normal vector to the interface with respect to c^- phase, which is given by $\mathbf{n}_s = \nabla c / |\nabla c|$. It is important to note that Eq. (21) can be used for both planar ($\kappa = 0$) and non-planar ($\kappa \neq 0$) interfaces. In fact, for both the planar and non-planar interfaces, we always have $|\nabla c| \simeq \sqrt{2\psi(c)}/\varepsilon \neq 0$ across the interface.

B. Coupling with hydrodynamic equations

To utilize the above phase-field model for computation of immiscible two-phase flows, the CH equation needs to be coupled with hydrodynamic equations, i.e., here the Navier–Stokes equation. Eulerian methods for computation of two-phase flows can be classified into multi-field approaches (such as the two-fluid model) and single-field approaches where the two phases share a common velocity field (Yeoh and Tu, 2010). As an interface-capturing method, the phase-field model naturally belongs to the latter category (Wörner, 2012).

1. Navier–Stokes equations

In order to close the equations governing the flow of two isothermal, immiscible, incompressible Newtonian fluids, the Cahn–Hilliard Eq. (21) is coupled with the Navier–Stokes equation comprising the conservation of mass (continuity) and the conservation of momentum (Abels *et al.*, 2012),

$$\nabla \cdot \mathbf{u} = 0, \tag{22}$$

$$\frac{\partial(\rho \mathbf{u})}{\partial t} + \nabla \cdot (\rho \mathbf{u} \otimes \mathbf{u}) = -\nabla p + \nabla \cdot \boldsymbol{\tau} - \frac{M}{2}(\rho^+ - \rho^-) \nabla \cdot (\mathbf{u} \otimes \nabla \phi) + \mathbf{f}_{\mathrm{b}} + \mathbf{f}_{\sigma}. \tag{23}$$

Here, $\mathbf{u}$ is the velocity field, t is the time, p is the pressure, and $\tau = \mu[(\nabla \mathbf{u}) + (\nabla \mathbf{u})^{\mathrm{T}}]$ is the viscous stress tensor for Newtonian fluids. The third term on the right-hand side of Eq. (23) is necessary to achieve thermodynamic consistency in the case of non-matched densities, although it vanishes in the case of matched densities (Abels *et al.*, 2012). In addition, ρ and μ are the fluid density and viscosity, respectively. Both depend linearly on the order parameter as

$$\begin{aligned} \rho(c) &= \frac{1}{2}\left[\rho^+(1+c) + \rho^-(1-c)\right], \\ \mu(c) &= \frac{1}{2}\left[\mu^+(1+c) + \mu^-(1-c)\right]. \end{aligned} \tag{24}$$

Furthermore, in Eq. (23), the term $\mathbf{f}_{\sigma}$ denotes the interfacial energy (per unit volume) while $\mathbf{f}_{\mathrm{b}}$ represents volumetric body forces (e.g., due to gravity).

2. Modified model for the interfacial energy density

In general, two different formulations for capillarity are used in combination with phase-field methods. These are the continuous surface force (CSF) model introduced by Brackbill *et al.* (1992) in the context of sharp-interface methods, and the Korteweg stress tensor representation inherent to diffuse interface methods (Anderson *et al.*, 1998; Antanovskii, 1995; and Espath *et al.*, 2016). Based on both approaches, quite different formulations for modeling the capillarity have been proposed in the literature (Guo *et al.*, 2021; Hua *et al.*, 2014; Kim, 2005; 2012; and Liu and Shen, 2003). Here, we follow the second approach, where the capillarity is modeled on the basis of the Korteweg stress tensor as (Gomez and van der Zee, 2017)

$$\mathbf{f}_{\sigma} = \frac{\partial \mathcal{F}[c]}{\partial(\nabla c)} \otimes \nabla c = -\lambda \nabla \cdot (\nabla c \otimes \nabla c). \tag{25}$$

The widely used standard interfacial energy density obtained from the Korteweg stress tensor is $\mathbf{f}_{\sigma}^{\mathrm{std}} = \phi \nabla c$ (Dinesh Kumar *et al.*, 2019; Zhang *et al.*, 2016; 2019). Vasilopoulos (2020) obtained a modified version of the standard interfacial tension force to more accurately account for interfacial tension effects. In the present work, we modified the standard interfacial energy density in a form different from that of Vasilopoulos (2020) as follows:

$$\mathbf{f}_{\sigma} = \mathbf{f}_{\sigma}^{\mathrm{std}} + \delta \mathbf{f}_{\sigma}, \tag{26}$$

where $\delta \mathbf{f}_{\sigma} = \mathbf{f}_{\sigma}^{\mathrm{std}} - \lambda \eta \nabla c$ is added to the standard capillarity to compensate for the deviation (if any) of the order parameter from an equilibrium profile. It is worth noting that theoretically the proposed Lagrange multiplier η will induce zero capillarity for any configuration (i.e., for planar and non-planar interfaces). However, when the numerical profile of the order parameter across the interface deviates from an equilibrium profile, a small but non-negligible interfacial energy density $\delta \mathbf{f}_{\sigma}$ will arise (Jamet and Misbah, 2008). In the numerical simulations carried out in the present work, it shall be shown that the additional term $\delta \mathbf{f}_{\sigma}$ decreases the difference between the analytical (Young-Laplace) and numerical pressure jump and thus increases accuracy.

C. Numerical implementation

In the bulk regions far from the interface, the term $|\nabla c|$ appearing in the denominator of the normal vector $\mathbf{n}_s$ approaches zero and hence some special treatment is needed in order to prevent a division by zero in numerical simulations. There have been few solutions proposed in the literature to overcome such a problem. For instance, in the VOF method, a very small but positive value is added to the denominator as $\delta_{\mathrm{VOF}} = 10^{-8} / \sqrt[3]{\sum_{i=1}^{N_{\mathrm{cell}}} V_i / N_{\mathrm{cell}}}$, where N_{cell} is the number of computational cells and V_i is the volume of individual cell

i (Vachaparambil and Einarsrud, 2019). In addition, Biben *et al.* (2005) proposed replacing the term $|\nabla c|$ with the term $\max(|\nabla c|, \delta_{\mathrm{PF}})$, where $\delta_{\mathrm{PF}} = 10^{-4}/(2\sqrt{2}\varepsilon)$ is called cutoff that is dependent on the capillary width ε.

In the present work, the following formula is used, which combines both aforementioned approaches:

$$\mathbf{n}_s = \frac{\nabla c}{|\nabla c| + \delta_{\mathrm{af}}}. \tag{27}$$

Here, the term $\delta_{\mathrm{af}} = 10^{-4}/(\sqrt{2}\varepsilon)$ not only prevents the denominator from becoming zero, but also unlike the aforementioned two methods, it does not lead to nonphysical spike formation in the pressure field within the interface.

The coupled CH-NS equations are solved in a segregated manner using the code phaseFieldFoam (PFF) developed in FOAM-extend 4. It may be noted that an earlier version of the code PFF has been used to study other aspects of the bubble and droplet dynamics using CH equation with standard chemical potential (see, for example, Cai *et al.*, 2015; 2016; 2017; Fink *et al.*, 2018; and Wörner *et al.*, 2021).

III. NUMERICAL RESULTS FOR TEST CASES IN STATIC EQUILIBRIUM

In this section, the performance of the method proposed in Sec. II is evaluated for the test case of a circular drop (radius r_0, diameter $d_0 = 2r_0$) in static equilibrium, which is a standard benchmark for two-phase flow solvers (Francois *et al.*, 2006; Herrmann, 2008; and Magnini *et al.*, 2016). Both phases are initially at rest and body forces are neglected ($\mathbf{f}_b = 0$). Results are presented for matched as well as non-matched density and viscosity ratios of the phases. The test case is discretized both in a 1D and a 2D setup, see Fig. 1. Numerical results are characterized with respect to (i) boundedness of the order parameter and phase mass conservation, (ii) parasitic currents, and (iii) Laplace pressure jump.

For a planar interface in equilibrium, the thickness of the diffuse interface is about $4\,\varepsilon$. In this paper, the resolution of the uniform grid (with mesh size h) is characterized by the number of mesh cells $N_{\mathrm{di}} = 4\varepsilon/h$ used to resolve the diffuse interface. The capillary width ε is determined indirectly by specifying a value for the Cahn number $Cn = \varepsilon/d_0$. Mobility $M = \chi\varepsilon^2$ is determined indirectly as well by fixing χ.

A. One-dimensional case with matched density and viscosity

For the 1D setup, a wedge-type computational domain is considered. The wedge has an opening angle of 5° and extends radially from $r = 0$ to $r = 2r_0$, where $r_0 = 0.5$ mm. The lateral sides of the wedge represent azimuthal symmetry planes, while at the outer radial boundary homogeneous Neumann conditions apply. The initial distribution of the order parameter is

$$c_0(r) = \tanh\left(\frac{r_0 - r}{\sqrt{2}\,\varepsilon}\right), \tag{28}$$

where r is the direction normal to the interface [see Fig. 1(a)]. Inside the drop, the order parameter thus takes positive values and negative values outside. The Cahn number is $Cn = 0.01$ and the mobility prefactor $\chi = 1\,\mathrm{m\,s\,kg^{-1}}$. The (matched) density and viscosity of the phases are $\rho^+ = \rho^- = 1\,\mathrm{kg\,m^{-3}}$ and $\mu^+ = \mu^- = 1$ Pa s. The coefficient of interfacial tension is $\sigma = 1\,\mathrm{N\,m^{-1}}$. The wedge is discretized in radial direction by 400 uniform mesh cells corresponding to $N_{\mathrm{di}} = 8$.

The variations of the order parameter in the direction normal to the interface at steady state ($t = 33$ ms) are depicted in Fig. 2. Results obtained with the standard chemical potential (ϕ_{std}) and the proposed chemical potential (ϕ_{af}) are compared with the initial analytical hyperbolic tangent profile c_0. While for ϕ_{std} the order parameter is not bounded, it is well bounded for ϕ_{af} where the profile of c at steady state agrees well with the analytical profile c_0. The relative errors in boundedness of c^+ are 0.47% and 0.000 18%, respectively. The corresponding values for c^- are 0.47% and 0.001%, respectively. Furthermore, while the interface position given by $c = 0$ is shifted inwards for ϕ_{std} (indicating mass loss of the drop phase), it stays located at r_0 for ϕ_{af} implying that the volume/mass of both phases is well conserved in this case.

B. Two-dimensional case with matched density and viscosity

For the 2D case, the drop with diameter $d_0 = 2$ mm is placed in the center of a square computational domain with size $2d_0 \times 2d_0$, see Fig. 1(b). At the borders of the computational domain, the zero-gradient boundary condition applies for the velocity, the order parameter, and the chemical potential, while pressure is fixed at zero. The origin of the Cartesian coordinate system (x, y) is located in the center of the drop and the initial distribution of the order parameter is given by

$$c_0(x, y) = \tanh\left(\frac{r_0 - \sqrt{x^2 + y^2}}{\sqrt{2}\,\varepsilon}\right). \tag{29}$$

As before, both phases are initially at rest. The density and viscosity of the phases are the same as in Sec. III A. For interfacial tension,

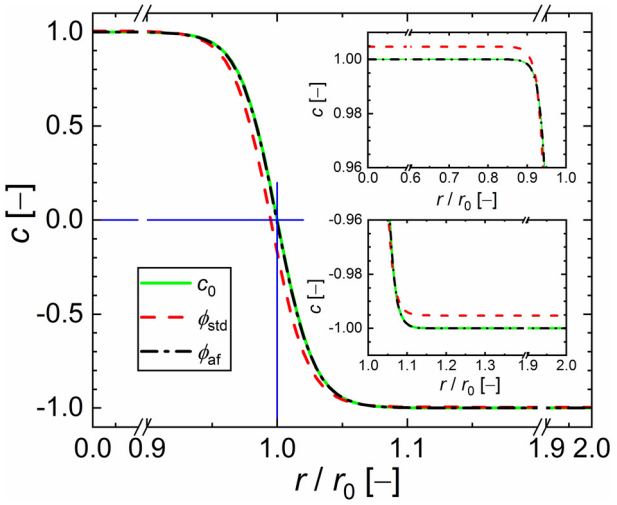

FIG. 2. Radial order parameter profiles for the 1D problem in a wedge-type geometry. Comparison of the computed order parameter at steady state ($t = 33$ ms) obtained by the standard and advected-field chemical potential with the analytical hyperbolic tangent profile c_0.

two different values $\sigma = 0.01$ and $\sigma = 0.1\,\mathrm{N\,m^{-1}}$ are considered, as most fluids have interfacial tension coefficients lying in between. Simulations are performed for a number of cases, where the Cahn number (Cn), the mobility pre-factor (χ), and the grid resolution (N_{di}) are varied.

1. Boundedness of order parameter

One of the most important features of a numerical method for multiphase flows simulation of immiscible fluids is its success in preserving the mass of the individual phases. For incompressible fluids considered here, mass conservation is equivalent to volume conservation. As mentioned in Sec. I, the CH equation with standard chemical potential does not generally preserve the mass of individual phases although it conserves the total mass of the system. In order to demonstrate that the proposed chemical potential ϕ_{af} conserves the mass of the individual phases, in this section, the deviation of the order parameter from the bulk values ± 1 for $\sigma = 0.1\,\mathrm{N\,m^{-1}}$, $Cn = 0.02$, and three different grid resolutions $N_{\mathrm{di}} = 4, 8, 16$ is depicted in Fig. 3, where $c_{\min}$ and $c_{\max}$ are, respectively, the minimum and maximum values of the order parameter in the computational domain. It is observed that for both ϕ_{std} and ϕ_{af} the boundedness for the fluid outside the droplet (here denoted by $c_{\min} + 1$) is more appreciated than for the fluid inside (here denoted by $c_{\max} - 1$). This may be attributed to the larger distance of the $c_{\min}$'s location(s) than the $c_{\max}$'s location(s) with respect to the interface ($c = 0$). It can also be seen that for the grid resolutions $N_{\mathrm{di}} = 8$ and $N_{\mathrm{di}} = 16$, the advected-field chemical potential ϕ_{af} results in bounded solution ($c_{\max} = 0.999\,997\,233\,5$ for $N_{\mathrm{di}} = 8$ and $c_{\max} = 1.000\,000\,573\,75$ for $N_{\mathrm{di}} = 16$), while ϕ_{std} violates the boundedness. In addition, although for $N_{\mathrm{di}} = 4$ the boundedness associated with ϕ_{af} has been significantly improved ($c_{\max} = 1.001\,312\,933$) with respect to ϕ_{std} case, using this grid resolution in two-phase flow simulations is not recommended. This figure substantiates the boundedness feature of the proposed chemical potential. It should be noted that a (relatively) higher violation of order parameter from its bulk values

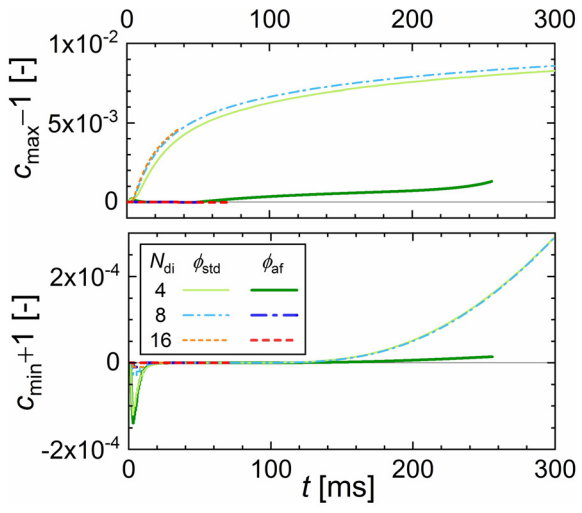

FIG. 3. Deviation of the order parameter from the bulk values ($\sigma = 0.1\,\mathrm{N\,m^{-1}}$, $Cn = 0.02$, $\chi = 0.1\,\mathrm{m\,s\,kg^{-1}}$).

using CH equation with standard chemical potential was reported by Jamshidi *et al.* (2019), where they used periodic boundary conditions.

2. Parasitic currents

In stagnant two phase flow problems where $\mathbf{u} = 0$ and in the absence of body forces, NS equation (23) reduces to $\nabla p = -\mathbf{f}_{\sigma}$, implying that the pressure gradient should be balanced by the interfacial tension force. Theoretically, the droplet and its surrounding fluid should remain motionless and no flow should be generated. In numerical simulations of such nominally stagnant flows, however, usually so-called parasitic currents (also known as spurious velocities) occur in various methods for interfacial computations of two-phase flows, as on the discrete level no equilibrium between the pressure and the capillarity is obtained. Two main sources for these numerical artifacts are as follows (Francois *et al.*, 2006): (i) employing not compatible discretization methods for pressure and capillarity terms and (ii) errors in the estimation of the local interface curvature κ. Different measures have been proposed in the literature to reduce parasitic currents. In the present work, the parasitic currents obtained by the standard and by the proposed chemical potentials are compared using the same discretization for the pressure gradient and capillarity terms in the two methods.

a. Effect of grid resolution. To study the effect of grid resolution on parasitic currents, simulations are performed for $\sigma = 0.1$ and $\sigma = 0.01\,\mathrm{N\,m^{-1}}$, keeping the Cahn number and the mobility parameter fixed ($Cn = 0.02$, $\chi = 0.1\,\mathrm{m\,s\,kg^{-1}}$). For each value of σ, three different grid resolutions corresponding to $N_{\mathrm{di}} = 4$, 8, and 16 are considered. As usual, parasitic currents are quantified by the maximum velocity magnitude $U_{\max}$ within the computational domain.

Figure 4(a) shows the time histories of $U_{\max}(t)$ obtained by both chemical potentials for interfacial tension coefficient $\sigma = 0.1\,\mathrm{N\,m^{-1}}$. For each chemical potential, the parasitic currents decrease with increasing grid resolution. In all cases, the parasitic currents initially jump to a high value at the beginning of the simulation from where they decrease in time. After reaching a minimum, $U_{\max}$ increases again. For ϕ_{af}, the parasitic currents always approach a certain steady state value $U^{\infty}_{\max}$. For ϕ_{std}, in contrast, no such steady parasitic currents are reached as can be seen in the inset of Fig. 4(a). It is noteworthy that to the authors' best of knowledge no previous study has reported steady state results for parasitic currents. In addition, for all the cases with ϕ_{af}, the higher parasitic currents including $U_{\max}$ remain always within the interface region. In contrast, for ϕ_{std}, the higher parasitic currents are initially concentrated around the interface but from a certain time they shift to the borders of the computational domain. While with ϕ_{std} smaller parasitic currents are obtained for a certain time interval as compared to ϕ_{af}, this cannot outweigh the distinct advantage of ϕ_{af} to achieve a steady state for $U_{\max}$. The time histories of $U_{\max}(t)$ for $\sigma = 0.01\,\mathrm{N\,m^{-1}}$ are shown in Fig. 4(b) for ϕ_{af} only. Again, the parasitic currents approach certain steady state values. According to Figs. 4(a) and 4(b), for all three grid resolutions, the respective values of $U^{\infty}_{\max}$ increase with increase in σ.

The steady parasitic currents can be quantified by the capillary number $Ca_{\mathrm{pc}} = \mu^{+} U^{\infty}_{\max}/\sigma$. Figure 5 depicts this capillary number against grid resolution (N_{di}) for the two interfacial tension coefficients considered. As simulations with ϕ_{std} do not converge to steady state

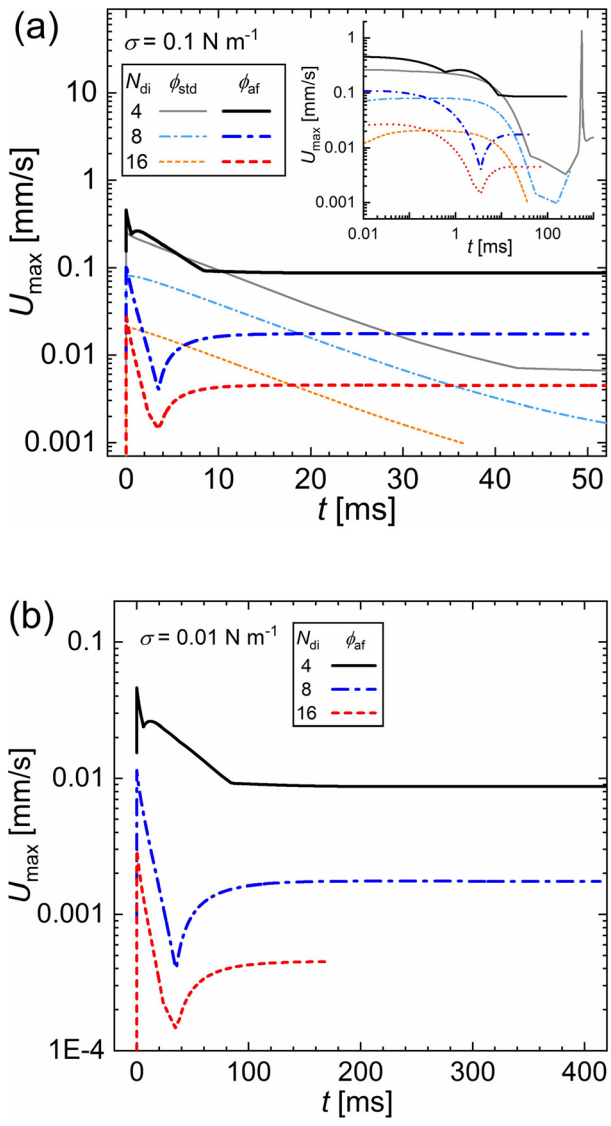

FIG. 4. Time history of the parasitic currents associated with the stagnant 2D droplet for (a) $\sigma = 0.1\,\mathrm{N\,m^{-1}}$ and (b) $\sigma = 0.01\,\mathrm{N\,m^{-1}}$ ($\chi = 0.1\,\mathrm{m\,s\,kg^{-1}}$, $Cn = 0.02$).

(equilibrium) solution, only the results associated with ϕ_{af} are given in Fig. 5. It can be observed that the results for both interfacial tension coefficients overlap and that the convergence rate of the proposed method concerning U^{∞}_{max} is about second order. The same convergence rate concerning parasitic currents given at a certain computational time rather than the steady state was reported by Jamshidi *et al.* (2019) where they employed the standard chemical potential in the CH equation along with periodic boundary conditions. Such a trend in convergence can also be deduced from Fig. 4(a) for ϕ_{std} at certain times of the simulation.

b. Effect of mobility parameter. The effect of mobility $M = \chi\varepsilon^2$ on the parasitic currents is investigated by considering three different

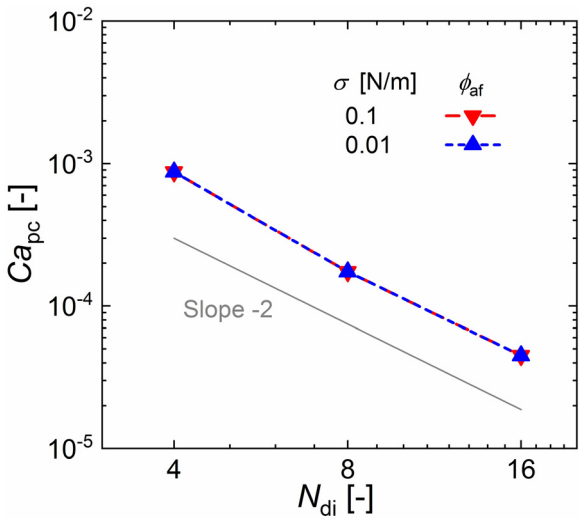

FIG. 5. Effect of mesh resolution on steady parasitic currents ($\chi = 0.1\,\mathrm{m\,s\,kg^{-1}}$, $Cn = 0.02$).

values of χ, namely, 0.01, 0.1, and 1 $\mathrm{m\,s\,kg^{-1}}$. Increasing χ increases the mobility coefficient M and hence the contribution of diffusion term in the CH equation. Consequently, the steady state (equilibrium) is reached faster. This is consistent with findings of Magaletti *et al.* (2013). In all cases, interface width is fixed as $\varepsilon = 2r_0Cn$, where $Cn = 0.02$ and $r_0 = 1$ mm. Grid resolution corresponds to $N_{di} = 8$. One could have expected that an increase in diffusion in the CH equation would result in dampening of parasitic currents. However, the opposite is true as U^{∞}_{max} increases with increase in χ and M as shown in Fig. 6. This finding of increasing the parasitic currents with χ and M

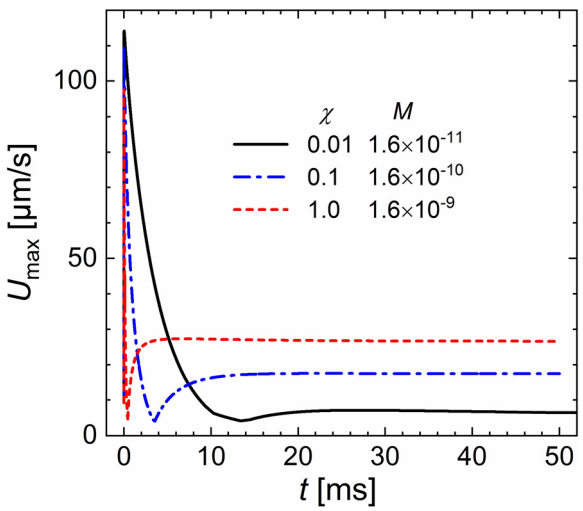

FIG. 6. Time history of parasitic currents for different values of mobility ($\sigma = 0.1\,\mathrm{N\,m^{-1}}$, $Cn = 0.02$, $N_{di} = 8$). Values of χ and M are given in units $\mathrm{m\,s\,kg^{-1}}$ and $\mathrm{m^3\,s\,kg^{-1}}$, respectively.

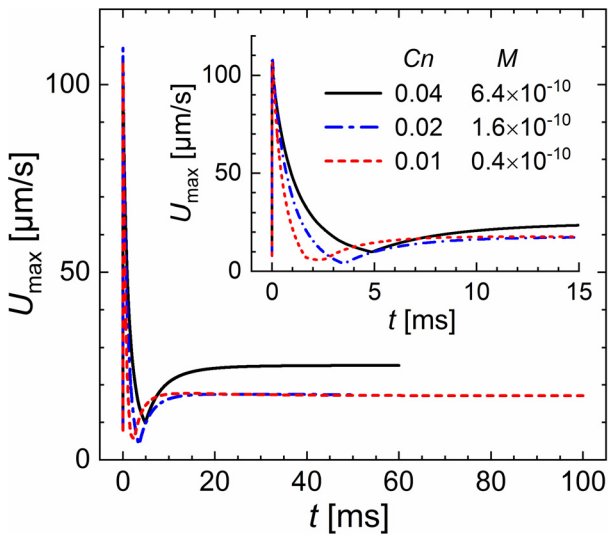

FIG. 7. Time history of parasitic currents for different Cahn numbers ($\sigma = 0.1\,\mathrm{N\,m^{-1}}$, $\chi = 0.1\,\mathrm{m\,s\,kg^{-1}}$, $N_{di} = 8$). Values of M are given in unit $\mathrm{m^3\,s\,kg^{-1}}$.

is consistent with that reported by Zu and He (2013), where they used the phase-field based lattice Boltzmann method.

c. Effect of Cahn number. The effect of Cahn number on the parasitic currents is studied by performing simulations with $Cn = 0.01$, 0.02, and 0.04 keeping $N_{di} = 8$ fixed. The results are given in Fig. 7. It can be seen that the steady parasitic currents are damped as the Cahn number decreases from $Cn = 0.04$ to $Cn = 0.02$. This can be explained as by definition $Cn = \varepsilon/d_0$, the Cahn number is proportional to the capillary width ε. Thus, decreasing Cn while keeping d_0 fixed results in a decrease in ε. For a fixed resolution of the diffuse interface $N_{di} = 4\varepsilon/h$, this would, then, result in a decrease in mesh size h. On the other hand, although the maximum parasitic current at steady state is about the same for $Cn = 0.01$ and $Cn = 0.02$, the case with smaller Cahn number requires more time to reach the steady state.

Table I depicts the steady values of parasitic currents and associated maximum and minimum values of the order parameter for the cases considered in Figs. 6 and 7. It can be seen that like the parasitic currents, the boundedness is also improved if the Cahn number and/or the mobility parameter χ decrease.

TABLE I. Steady parasitic currents and the associated order parameter for different values of Cn number and χ ($\sigma = 0.1\,\mathrm{N\,m^{-1}}$, $N_{di} = 8$).

Cn	χ	U^{∞}_{max} ($\mu\mathrm{m\,s^{-1}}$)	$c_{min}(-)$	$c_{max}(-)$
0.01		17.1	−1.000 000 000 0	1.000 085 471 0
0.02	0.1	17.4	−1.000 000 001 0	0.999 997 233 5
0.04		25.2	−0.999 999 809 5	0.999 908 538 6
	0.01	5.3	−1.000 000 001 0	0.999 995 847 5
0.02	0.1	17.4	−1.000 000 001 0	0.999 997 233 5
	1.0	26.6	−0.999 976 739 1	1.000 117 819 0

3. Pressure jump

For analysis of the pressure jump, simulation results with fixed values $Cn = 0.02$, $N_{di} = 8$, $\chi = 0.1\,\mathrm{m\,s\,kg^{-1}}$, and $r_0 = 1\,\mathrm{mm}$ are utilized. The relative error of the pressure jump is defined here as $E_{rel} = |\Delta p_{num} - \Delta p_{YL}|/\Delta p_{YL}$, where $\Delta p_{YL} = \sigma/r_0$ and Δp_{num} are the analytical Young–Laplace and numerical pressure jump, respectively. The numerical pressure jump is evaluated as the difference between the pressure at the center of the droplet and the pressure outside the droplet far away from the interface. It is worth noting that in the simulations the pressure profile initially experiences a nonphysical peak at the interface. However, this pressure peak vanishes as the steady state for parasitic currents is achieved. The error percentage in the pressure jump at the instance of steady state against grid resolution is depicted in Fig. 8. It is evident that for both values of interfacial tension coefficient (i.e., $\sigma = 0.01$ and $\sigma = 0.1\,\mathrm{N\,m^{-1}}$), the proposed chemical potential along with the modified capillarity returns very accurate results for pressure jump. The rate of convergence with mesh refinement is about third order.

It is worth noting that the present modified interfacial energy density formulation [Eq. (26)] results in more accurate pressure jump between the two phases than the standard interfacial energy density formulation $\mathbf{f}^{std}_{\sigma}$ when they are used in conjunction with the proposed chemical potential. In fact, without the correction term added to the standard interfacial energy density, the proposed chemical potential underestimates the pressure gradient more than the standard chemical potential. In order to demonstrate the effect of the correction term on the pressure jump, the pressure profile associated with the stagnant droplet with matched density and viscosity is depicted in Fig. 9, where the interfacial tension coefficient $\sigma = 0.1\,\mathrm{N\,m^{-1}}$ pertaining to the analytical pressure jump value 100 Pa is considered. It can be seen that the pressure jump obtained using $\mathbf{f}_{\sigma}$ is equal to $99.754\,\mathrm{N\,m^{-2}}$ that is more accurate than $98.583\,\mathrm{N\,m^{-2}}$ obtained by $\mathbf{f}^{std}_{\sigma}$.

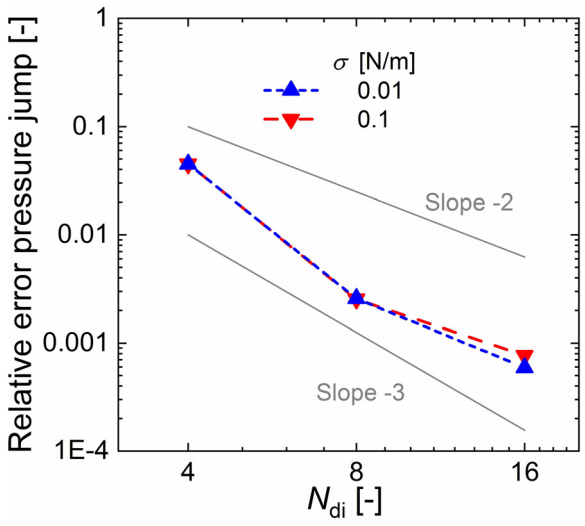

FIG. 8. Error in pressure jump vs grid resolution for the proposed chemical potential ($Cn = 0.02$, $\chi = 0.1\,\mathrm{m\,s\,kg^{-1}}$).

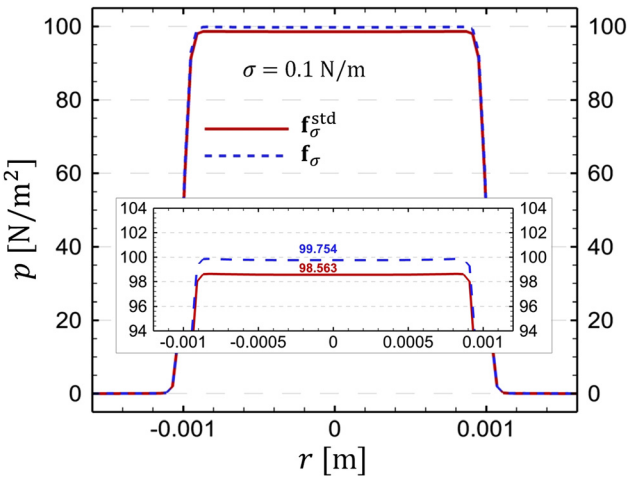

FIG. 9. Effect of capillarity formulation on the pressure jump between two phases using present chemical potential ($\sigma = 0.1\,\text{N m}^{-1}$, $Cn = 0.02$, $N_{\text{di}} = 8$, $\chi = 0.1\,\text{m s kg}^{-1}$).

C. Two-dimensional case with water–air properties

In order to substantiate the applicability of the proposed chemical potential in the simulation of problems with real physical properties of the phases, in this section, a two-dimensional stagnant problem with the same configuration as in Sec. III B is considered but now for a water droplet in ambient air. The physical properties include density $\rho^+ = 998$, $\rho^- = 1.29\,\text{kg m}^{-3}$, kinematic viscosity $\nu^+ = 9.03 \times 10^{-7}$, $\nu^- = 1.48 \times 10^{-5}$ $\text{m}^2\,\text{s}^{-1}$, and interfacial tension coefficient $\sigma = 0.072\,\text{N m}^{-1}$. In addition, we consider $Cn = 0.02$, $\chi = 0.1\,\text{m s kg}^{-1}$, and $N_{\text{di}} = 8$. The results are demonstrated in Fig. 10. It can be seen that with the chemical potential ϕ_{af} the parasitic currents have reached a steady (equilibrium) state, while for the standard chemical potential, U_{max} is oscillatory. In addition, although for the standard chemical potential ϕ_{std} the average value of the parasitic currents become smaller than the proposed method from a certain time (∼43 ms), they increase again from $t \sim 97$ ms and reach a maximum of ∼44 mm s^{-1} at $t \sim 268$ ms before they decrease again (not shown). As shown in supplementary material, for ϕ_{af}, the higher parasitic currents including U_{max} are restricted to the interface region, while for ϕ_{std} they initially appear around the interface, but start to shift to the borders of the computational domain from a certain time (here $t \sim 92$ ms). Therefore, the comparison of the terminal parasitic currents in the two methods is again unreasonable.

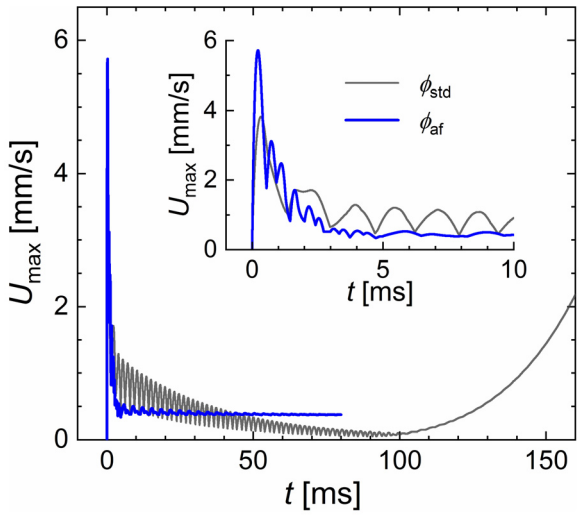

FIG. 10. Variations of the maximum parasitic current with time for water droplet in air ($\sigma = 0.072\,\text{N m}^{-1}$, $\chi = 0.1\,\text{m s kg}^{-1}$, $Cn = 0.02$, $N_{\text{di}} = 8$).

D. Two droplets of different sizes in a stagnant fluid

In this section, we consider a case with two droplets of different sizes immersed in a stagnant fluid. The physical properties of the primary phase and the dispersed phase (droplets) as well as the boundary conditions are considered identical to those in Sec. III B. In addition, $Cn = 0.02$ and $N_{\text{di}} = 8$. Two droplets with initial radii of $r_0^{\text{l}} = 1$ and $r_0^{\text{s}} = r_0^{\text{l}}/4 = 0.25$ mm are placed in a $3d_0^{\text{l}} \times 2d_0^{\text{l}}$ rectangular computational domain (see Fig. 11). The initial center points of the larger and smaller droplets given in units of mm are $\text{C}_{\text{l}}(-1, 0)$ and $\text{C}_{\text{s}}(0.75, 0)$, respectively, and the corners of the computational domain are $\text{A}(-3, -2)$, $\text{B}(3, -2)$, $\text{C}(-3, 2)$, and $\text{D}(3, 2)$.

The results are depicted in Fig. 12 at three different times of $t = 0$, 100, and 242 ms. It can be seen that with the standard chemical potential, the droplets shift leftward, presumably due to the parasitic currents, and they experience a decrease in their size. The decrease in radius $\delta r/r_0$ (or area $\delta A/A_0 = \pi[r_0^2 - r^2]/(\pi r_0^2)$) of the smaller droplet is 4.8 (9.37)% and 8.0 (15.36)%, respectively, at times $t = 100$ and 242 ms. The corresponding values for the larger droplet are 0.2 (0.399)% and 0.4 (0.798)%, respectively. Therefore, the volume/mass of the droplets (and hence the individual phases) are not conserved. In addition, the center of the smaller droplet shifts about 0.026 and 0.121 mm leftward at times $t = 100$ and 242 ms, respectively. These values are 0.019 and 0.104 mm for the larger droplet. In the proposed method using the chemical potential ϕ_{af}, however, both the droplets remain fixed without any change in their size and position (not shown therefore). This implies that the volume/mass of the droplets (and hence the individual phases) are conserved. This test case further

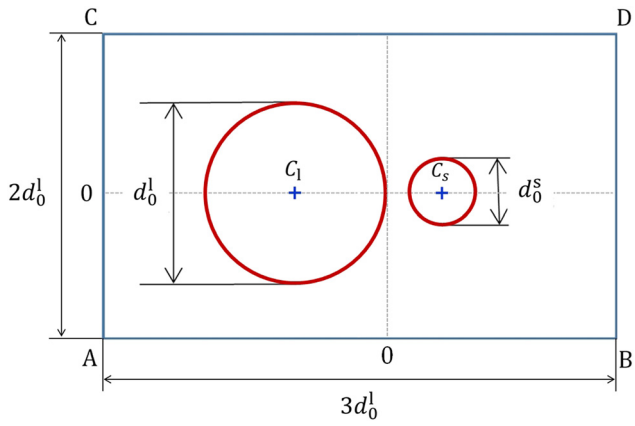

FIG. 11. Schematic representation of two droplets in a stagnant immiscible fluid.

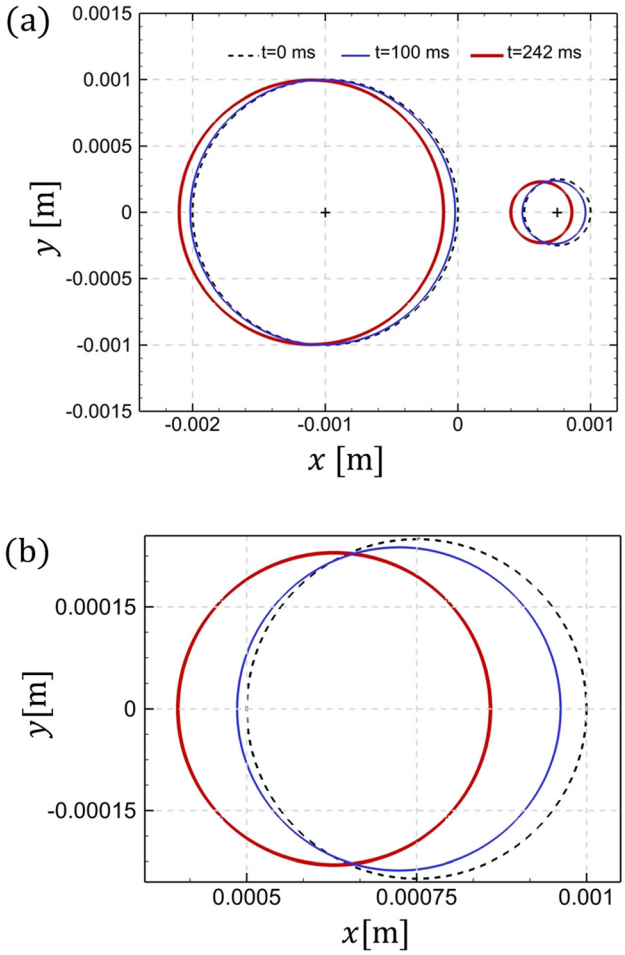

FIG. 12. Two stagnant droplets of different sizes simulated using ϕ_{std} at three different times. (a) The droplets shift leftward and become smaller and (b) smaller droplet at times 0, 100, and 242 ms.

demonstrates that the proposed chemical potential avoids any curvature driven motion even for multiple interfaces exhibiting different values of curvature. It may be noted that the problem of two stationary disks/droplets was also studied by Chai *et al.* (2018) using local and non-local AC equations with mass conservation, where no apparent changes in the radii of the two disks during the time evolution were observed.

IV. DROP DEFORMATION IN CONFINED SHEAR FLOW

Thus far we evaluated the efficiency of the proposed chemical potential through the consideration of four test cases where the bulk velocity of the two phases is zero, i.e., $\mathbf{u}(x, y, z) = 0$. In this section, a test case is considered where the bulk flow is not stagnant. To this end, the droplet deformation in a shear flow (sf) driven by two parallel plates moving with constant speed U in opposite directions is simulated.

The physical configuration of this problem is shown in Fig. 13. No-slip boundary condition is applied to the plates, while periodic

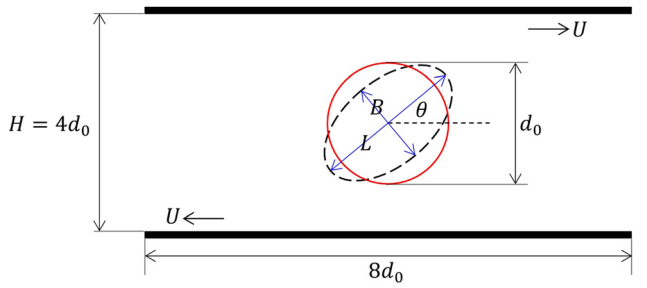

FIG. 13. Schematic of drop deformation in a shear flow.

boundary condition is implemented on the left and right boundaries. Matched density and viscosity of the phases, i.e., $\rho^+ = \rho^- = 1$ kg m^{-3} and $\mu^+ = \mu^- = 1$ Pa s are considered. Three cases distinguished by different values of capillary number Ca_{sf} of 0.1, 0.3, and 0.5 are examined. In all the cases considered in this section, the Reynolds number Re_{sf} is fixed at 0.1. Here, the capillary and Reynolds numbers are defined as $Ca_{\text{sf}} = \mu r_0 \dot{\gamma}/\sigma$ and $Re_{\text{sf}} = \rho r_0^2 \dot{\gamma}/\mu$, where $\dot{\gamma} = U/(4r_0)$ is the shear rate and r_0 is the radius of the initial circular droplet.

In the phase-field method, the interface should be well resolved for interfacial effects to be computed accurately and to approach the sharp interface limit. While the result presented in Sec. III was obtained on uniform grids, achieving a steady state solution of the droplet deformation in shear flow using uniform mesh needs more computational time as compared to the case of stagnant droplet. Furthermore, as drop deformation increases with Ca_{sf}, the computational time also increases with capillary number since it takes more time to reach the steady state. To achieve high numerical accuracy with moderate computational cost, here local adaptive mesh refinement (AMR) library (Rettenmaier *et al.*, 2019) is used, which allows us to provide higher mesh densities where needed, i.e., here at the interface.

Starting from an initial circular shape, the droplet deforms gradually until the overall shear force exerted on it is balanced by the capillarity and it reaches a steady state. The amount of deformation of the drop at steady state is determined by Ca_{sf} and Re_{sf}. The droplet shapes for three different Ca_{sf} numbers of 0.1, 0.3, and 0.5 and constant Re_{sf} of 0.1 for which the steady state solutions have been reached are depicted in Fig. 14 accompanied by the corresponding AMR. It can be seen that with increase in Ca_{sf} the droplet gets more slender while the inclination decreases.

The numerical results for the steady drop shape and inclination (i.e., the angle θ in Fig. 13) are compared with available theoretical and numerical counterparts. The drop shape is quantified by the deformation parameter

$$D = \frac{L - B}{L + B}, \tag{30}$$

where L and B denote the dimensions of the major and minor axes of the droplet, respectively. The time history of the deformation parameter for the three different values of Ca_{sf} is displayed in Fig. 15. For the lowest capillary number, the steady drop deformation is reached after about 2 s, whereas for the largest value of Ca_{sf} up to 12 s are needed.

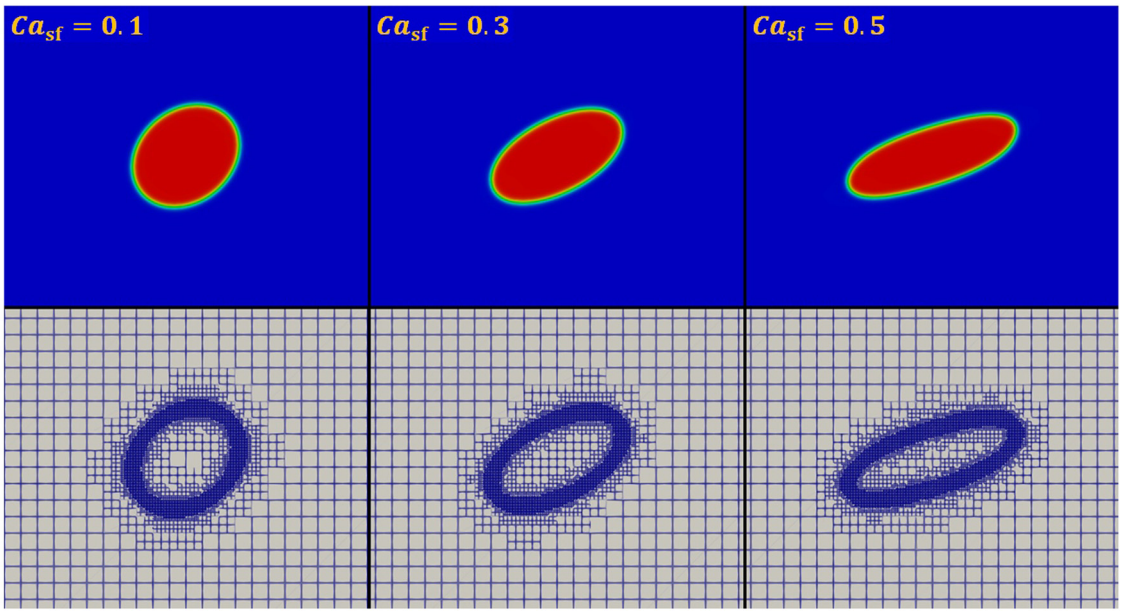

FIG. 14. Droplet shapes at steady-state in shear flow ($Re_{sf} = 0.1$) for different values of Ca_{sf} number.

A theoretical solution for the (steady) deformation parameter D in this problem is given by Cox (1969) as follows:

$$D = \frac{5(16 + 19\xi)}{4(1 + \xi)\sqrt{(20/Ca_{sf})^2 + (19\xi)^2}}, \tag{31}$$

where the viscosity ratio $\xi = \mu^+/\mu^-$ with μ^+ and μ^- being the dynamic viscosity of the droplet and surrounding fluid, respectively. Maffettone and Minale (1998) proposed the following expression for the orientation angle based on a simple phenomenological model:

$$\theta = \frac{1}{2}\arctan\left(\frac{40(1 + \xi)}{Ca_{sf}(3 + 2\xi)(16 + 19\xi)}\right). \tag{32}$$

It has been proved that there is a good agreement between the model proposed by Maffettone and Minale (1998) and the experimental results in unbounded flows (Vananroye *et al.*, 2007). This model and the model proposed by Cox (1969) are not expected to be valid in confined flows since they are not functions of the gap distance between the walls. The model of Shapira and Haber (1990) (SH), however, takes into account the wall effects as

$$D_{SH} = D_{Taylor}\left[1 + C_{SH}\frac{1 + 2.5\xi}{1 + \xi}\left(\frac{r_0}{H}\right)^3\right], \tag{33}$$

where H is the gap distance between the walls and C_{SH} represents a shape factor, which depends on the position of the droplet relative to the walls. If the droplet is positioned exactly in the middle between the two walls $C_{SH} = 5.699\,6$. In Eq. (33), D_{Taylor} represents the correlation proposed by Taylor (1934) for the deformation parameter given by

$$D_{Taylor} = \frac{16 + 19\xi}{16 + 16\xi}Ca_{sf}. \tag{34}$$

Unlike for the deformation parameter, no influence of confinement on the inclination angle θ is reported in the literature.

The results for the steady deformation parameter D and orientation angle θ are depicted in Figs. 16 and 17, respectively. In addition to analytical results, the present results are compared with numerical results obtained by Yuan *et al.* (2017), where PFSF stands for phase-field-based surface tension force and FESF stands for free energy-based surface tension force. It can be seen that there is a good agreement between the current results and the corresponding analytical and numerical results. Table II gives the area of the droplet and the maximum and minimum values of the order parameter in the

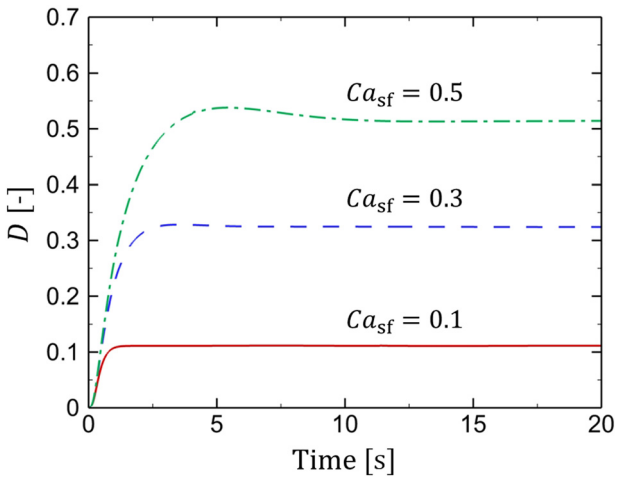

FIG. 15. Evolution of droplet deformation in shear flow ($Re_{sf} = 0.1$) for different values of Ca_{sf} number.

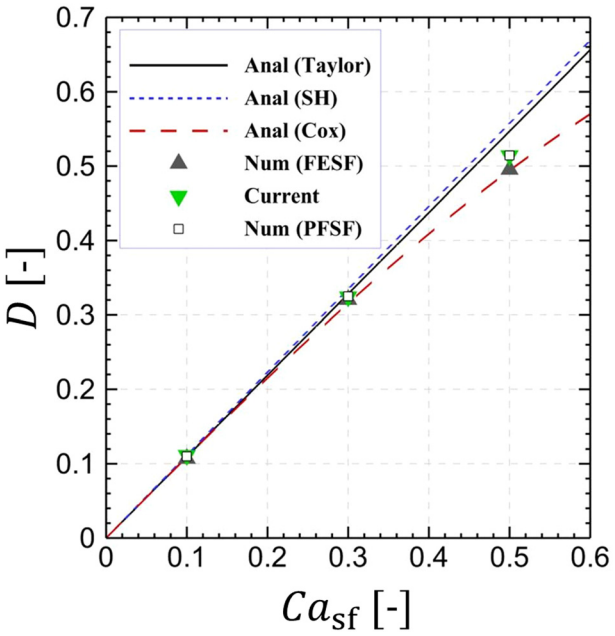

FIG. 16. Deformation parameter vs Ca_{sf} for droplet deformation in a shear flow ($Re_{sf} = 0.1$).

computational domain at steady state. The maximum deviation of the droplet area at steady state from its initial area (314.984 558 5 mm^2) is equal to 0.272% pertaining to the case with $Ca_{sf} = 0.5$, which is very small. This would justify, once again, that the order parameter is well-bounded and hence the volume/mass of the individual phases is conserved.

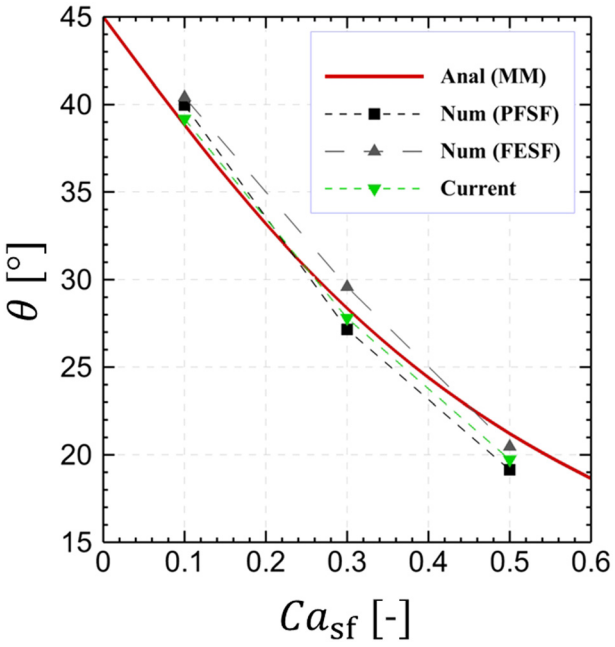

FIG. 17. Orientation angle vs Ca_{sf} for droplet deformation in a shear flow ($Re_{sf} = 0.1$).

TABLE II. Area of the droplet in shear flow ($Re_{sf} = 0.1$) at steady state and the deviation from its initial area for different values of Ca_{sf} number.

Ca_{sf}	A_{steady} (mm^2)	Error in area (%)	c_{min} (−)	c_{max} (−)
0.1	314.194 184 62	0.011	−1.000 73	1.001 17
0.3	313.526 003 78	0.201	−1.006 47	1.008 21
0.5	313.305 892 15	0.272	−1.009 42	1.016 50

V. CONCLUSIONS

Despite its vast success in simulating incompressible multiphase flows, the Cahn–Hilliard phase-field model still suffers from the drawback of non-conserving the volume of individual phases. To overcome this drawback, a curvature-dependent chemical potential for the Cahn–Hilliard equation is proposed that allows for stationary solutions for drops/bubbles having uniform non-zero curvature. The proposed chemical potential along with a modified interfacial energy density was implemented in FOAM-extend 4.0 with special treatment of the normal unit vector and applied to various static and dynamic immiscible two-phase problems. It was found that the proposed chemical potential has significant advantages as compared to standard chemical potential. Most importantly, the proposed chemical potential gives rise to bounded solution for the order parameter and hence preserves well the volume/mass of the individual phases, while the standard chemical potential does not. Due to improved boundedness, the proposed method is also more compatible (stable) than the standard one when order parameter based adaptive mesh refinement is used.

In addition, the effect of Cahn number, mobility coefficient, and mesh resolution on the parasitic currents associated with the static cases has been examined. The results revealed that with the proposed chemical potential, the Cahn–Hilliard Navier–Stokes equations always converge to steady state solutions for nominally stagnant cases, while the steady state solution will not be reached with the standard chemical potential. The parasitic currents decrease with mesh refinement. Smaller Cahn number leads to slower convergence but smaller parasitic currents. Larger mobility leads to a faster convergence at the expense of higher parasitic currents.

In the case of two stagnant droplets immersed in a stagnant immiscible liquid, the proposed method preserves both the volume and position of individual droplets. However, this is not the case in the original method. In addition, comparison of the results of the dynamic droplet deformation in shear flow for three capillary numbers with the available analytical and numerical data demonstrates good agreement. The area of the droplet after deformation is well preserved confirming again the boundedness feature of the proposed method.

Overall, the proposed method which is based on the thermodynamically consistent advected-field chemical potential gives rise to stable, converged, and bounded solutions.

SUPPLEMENTARY MATERIAL

See the supplementary material for the contour plots of the parasitic currents related to Fig. 10.

ACKNOWLEDGMENTS

The authors acknowledge financial support from the German Research Foundation (Deutsche Forschungsgemeinschaft, DFG) through Project No. 237267381-TRR 150. Calculations for this research were conducted on bwUniCluster funded by the Ministry of Science, Research, and the Arts Baden-Württemberg and DFG ("Deutsche Forschungsgemeinschaft") within the framework program bwHPC and on the Lichtenberg High Performance Computer of the TU Darmstadt.

APPENDIX: ANALYTICAL AND NUMERICAL SOLUTION OF THE STEADY CH EQUATION

In this section, analytical and numerical solutions of Eq. (8) for an axisymmetric 2D problem (where $N=2$ and the order parameter c varies only in the directions normal to the interface r) are given and discussed briefly. It shall be shown that adding $\eta = const.$ to Eq. (8) gives an oscillatory solution of this equation. In the analytical solution, following Wazwaz *et al.* (2013), we use the Adomian decomposition method (ADM) (Adomian and Rach, 1983) to solve the Volterra integral form of the equation. This equation is, actually, of the form of the well-known Lane–Emden equation of shape factor $k = N - 1$,

$$c''(r) + \frac{k}{r}c'(r) + f(c) = 0, \quad c(0) = \alpha, \quad c'(0) = 0, \quad k \geq 0, \tag{A1}$$

where $f(c)$ is a nonlinear term. Adding η to Eq. (8), the nonlinear term $f(c)$ in Eq. (A1) takes the form

$$f(c) = \frac{1}{\varepsilon^2}\psi'(c) + \eta. \tag{A2}$$

The Volterra integral form of Eq. (A1) is written as

$$c(r) = \alpha + \int_0^r t \ln\left(\frac{t}{r}\right) f(c(t))\,\mathrm{d}t. \tag{A3}$$

The ADM uses the following infinite decomposition series:

$$c(r) = \sum_{n=0}^{\infty} c_n(r) \tag{A4}$$

for the solution $c(r)$ and the following infinite series of polynomials:

$$f(c) = \sum_{n=0}^{\infty} A_n(c_0, c_1, \ldots, c_n) \tag{A5}$$

for the nonlinear term $f(c)$ where the components $c_n(r)$ of the solution $c(r)$ will be determined recurrently. In addition, A_n are the Adomian polynomials, which are obtained in a recurrence procedure as (Duan, 2011)

$$A_n = \sum_{i=1}^{n} D_n^i f^{(i)}(c_0), \quad n \geq 1, \tag{A6}$$

where $D_n^1 = c_n,\ n \geq 1$ and $D_n^i = \frac{1}{n}\sum_{i=1}^{n}(j+1)c_{j+1}D_{n-1-j}^{i-1}$, $2 \leq i \leq n$.

Substituting Eqs. (A4) and (A5) into Eq. (A3) yields

$$\sum_{n=0}^{\infty} c_n(r) = \alpha + L^{-1}\left(\sum_{n=0}^{\infty} A_n(c_0, c_1, \ldots, c_n)\right), \tag{A7}$$

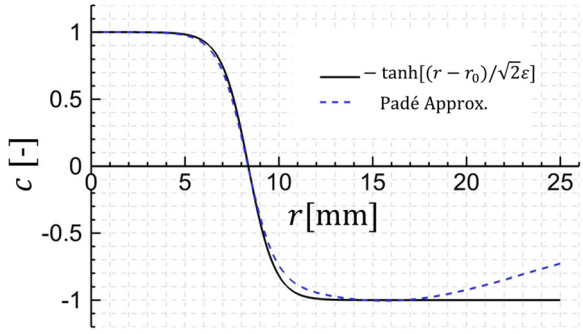

FIG. 18. The Padé approximants $\{[11/12]\, y_{12}(r)\}$ compared to the hyperbolic tangent profile.

where $L^{-1}(g(r)) = \int_0^r t \ln\left(\frac{t}{r}\right) g(t)\,\mathrm{d}t$. Therefore, we have

$$\begin{aligned} c_0(r) &= \alpha, \\ c_{j+1}(r) &= L^{-1}(A_j), \quad j \geq 0. \end{aligned} \tag{A8}$$

The obtained series solution is as follows:

$$c(r) = B_0 + \sum_{n=1}^{\infty} c_n(r) = B_0 - \sum_{n=1}^{\infty} \frac{B_n(r)}{(2n)^2} r^{2n}, \tag{A9}$$

where $B_0 = c_0 = \alpha$, $B_1 = f(c_0)$, $B_2 = f'(c_0)B_1$, $B_3 = f'(c_0)B_2 + f''(c_0)\left(\frac{1}{2}B_1^2\right)$, etc. It can easily be shown that the coefficients B_n, $n \geq 2$ have, respectively, the same form as those for A_{n-1}, $n \geq 2$ with the only difference that c_i terms in A_n are replaced with the terms B_i, i.e., $B_n = A_{n-1}|_{c_i = B_i}$. We denote the m-term approximant of the series solution of $c(r)$ as $y_{12}(r) = \sum_{j=0}^{12} c_j(r)$ and plot in Fig. 18 the curve of the Padé approximants $\{[11/12]\, y_{12}(r)\}$ against $-\tanh[(r - r_0)/(\sqrt{2}\,\varepsilon)]$. In this figure $\varepsilon = 1$ and $\eta = 0.000\,27$, for which $R_0 = 8.37$ mm is obtained. It is worth mentioning that the value of η depends on both R_0 and ε. It can be seen that using the constant value for η, the solution of Eq. (A1) does not satisfy the boundary condition $c'(\infty) = 0$ and in the meantime it becomes oscillatory.

It should be noted that the same result has been obtained by solving Eq. (A1) numerically using the fourth order-Runge Kutta method.

DATA AVAILABILITY

The data that support the findings of this study are available from the corresponding author upon reasonable request.

REFERENCES

Abels, H., Depner, D., and Garcke, H., "On an incompressible Navier–Stokes/Cahn–Hilliard system with degenerate mobility," Ann. Inst. Henri Poincare **30**, 1175–1190 (2013).

Abels, H., Garcke, H., and Grün, G., "Thermodynamically consistent, frame indifferent diffuse interface models for incompressible two-phase flows with different densities," Math. Models Methods Appl. Sci. **22**, 1150013 (2012).

Adomian, G., and Rach, R., "Inversion of nonlinear stochastic operators," J. Math. Anal. Appl. **91**, 39–46 (1983).

Aland, S., "Modelling of two-phase flow with surface active particles," Ph.D. thesis (Technical University of Dresden, 2012).

Alfaro, M., and Alifrangis, P., "Convergence of a mass conserving Allen–Cahn equation whose Lagrange multiplier is nonlocal and local," Interfaces Free Boundaries **16**, 243–268 (2014).

Allen, S. M., and Cahn, J. W., "A microscopic theory for antiphase boundary motion and its application to antiphase domain coarsening," Acta Metall. **27**, 1085–1095 (1979).

Anderson, D. M., McFadden, G. B., and Wheeler, A. A., "Diffuse-interface methods in fluid mechanics," Annu. Rev. Fluid Mech. **30**, 139–165 (1998).

Antanovskii, L. K., "A phase field model of capillarity," Phys. Fluids **7**, 747–753 (1995).

Badalassi, V., Ceniceros, H., and Banerjee, S., "Computation of multiphase systems with phase field models," J. Comput. Phys. **190**, 371–397 (2003).

Biben, T., Kassner, K., and Misbah, C., "Phase-field approach to three-dimensional vesicle dynamics," Phys. Rev. E **72**, 041921 (2005).

Biben, T., Misbah, C., Leyrat, A., and Verdier, C., "An advected-field approach to the dynamics of fluid interfaces," Europhys. Lett. **63**, 623–629 (2003).

Bonart, H., Jung, J., Kahle, C., and Repke, J. U., "Influence of liquid density and surface tension on the pinning of sliding droplets on a triangular microstructure," Chem. Eng. Technol. **42**, 1381–1387 (2019a).

Bonart, H., Kahle, C., and Repke, J. U., "Comparison of energy stable simulation of moving contact line problems using a thermodynamically consistent Cahn–Hilliard Navier–Stokes model," J. Comput. Phys. **399**, 108959 (2019b).

Boyer, F., "Mathematical study of multi-phase flow under shear through order parameter formulation," Asymptotic Anal. **20**, 175–212 (1999).

Brackbill, J. U., Kothe, D. B., and Zemach, C., "A continuum method for modeling surface tension," J. Comput. Phys. **100**, 335–354 (1992).

Brassel, M., and Bretin, E., "A modified phase field approximation for mean curvature flow with conservation of the volume," Math. Methods Appl. Sci. **34**, 1157–1180 (2011).

Cahn, J. W., and Hilliard, J. E., "Free energy of a nonuniform system. I. Interfacial free energy," J. Chem. Phys. **28**, 258–267 (1958).

Cai, X., Marschall, H., Wörner, M., and Deutschmann, O., "Numerical simulation of wetting phenomena with a phase-field method using OpenFOAM®," Chem. Eng. Technol. **38**, 1985–1992 (2015).

Cai, X., Wörner, M., Marschall, H., and Deutschmann, O., "Numerical study on the wettability dependent interaction of a rising bubble with a periodic open cellular structure," Catal. Today **273**, 151–160 (2016).

Cai, X., Wörner, M., Marschall, H., and Deutschmann, O., "CFD simulation of liquid back suction and gas bubble formation in a circular tube with sudden or gradual expansion," Emiss. Control Sci. Technol. **3**, 289–301 (2017).

Ceniceros, H. D., and García-Cervera, C. J., "A new approach for the numerical solution of diffusion equations with variable and degenerate mobility," J. Comput. Phys. **246**, 1–10 (2013).

Chai, Z., Sun, D., Wang, H., and Shi, B., "A comparative study of local and nonlocal Allen–Cahn equations with mass conservation," Int. J. Heat Mass Transfer **122**, 631–642 (2018).

Chatzidai, N., Giannousakis, A., Dimakopoulos, Y., and Tsamopoulos, J., "On the elliptic mesh generation in domains containing multiple inclusions and undergoing large deformations," J. Comput. Phys. **228**, 1980–2011 (2009).

Chiu, P. H., and Lin, Y. T., "A conservative phase field method for solving incompressible two-phase flows," J. Comput. Phys. **230**, 185–204 (2011).

Cox, R., "The deformation of a drop in a general time-dependent fluid flow," J. Fluid Mech. **37**, 601–623 (1969).

Dai, S., and Du, Q., "Weak solutions for the Cahn–Hilliard equation with degenerate mobility," Arch. Ration. Mech. Anal. **219**, 1161–1184 (2016).

Dinesh Kumar, E., Sannasiraj, S., and Sundar, V., "Phase field lattice Boltzmann model for air–water two phase flows," Phys. Fluids **31**, 072103 (2019).

Ding, H., and Yuan, C. J., "On the diffuse interface method using a dual-resolution Cartesian grid," J. Comput. Phys. **273**, 243–254 (2014).

Duan, J. S., "Convenient analytic recurrence algorithms for the Adomian polynomials," Appl. Math. Comput. **217**, 6337–6348 (2011).

Elliott, C. M., and Garcke, H., "On the Cahn–Hilliard equation with degenerate mobility," Siam J. Math. Anal. **27**, 404–423 (1996).

Espath, L. F. R., Sarmiento, A. F., Vignal, P., Varga, B., Cortes, A. M. A., Dalcin, L., and Calo, V. M., "Energy exchange analysis in droplet dynamics via the Navier–Stokes–Cahn–Hilliard model," J. Fluid Mech. **797**, 389–430 (2016).

Fink, V., Cai, X., Stroh, A., Bernard, R., Kriegseis, J., Frohnapfel, B., Marschall, H., and Wörner, M., "Drop bouncing by micro-grooves," Int. J. Heat Fluid Flow **70**, 271–278 (2018).

Folch, R., Casademunt, J., Hernández-Machado, A., and Ramírez-Piscina, L., "Phase-field model for Hele-Shaw flows with arbitrary viscosity contrast. II. Numerical study," Phys. Rev. E **60**, 1734–1740 (1999).

Francois, M. M., Cummins, S. J., Dendy, E. D., Kothe, D. B., Sicilian, J. M., and Williams, M. W., "A balanced-force algorithm for continuous and sharp interfacial surface tension models within a volume tracking framework," J. Comput. Phys. **213**, 141–173 (2006).

Fuster, D., Agbaglah, G., Josserand, C., Popinet, S., and Zaleski, S., "Numerical simulation of droplets, bubbles and waves: State of the art," Fluid Dyn. Res. **41**, 065001 (2009).

Geier, M., Fakhari, A., and Lee, T., "Conservative phase-field lattice Boltzmann model for interface tracking equation," Phys. Rev. E **91**, 063309 (2015).

Gomez, H., and van der Zee, K. G., "Computational phase-field modeling," in *Encyclopedia of Computational Mechanics, 2nd ed.*, edited by Stein, E., Borst, R., and Hughes, T. J. R. (American Cancer Society, 2017), pp. 1–35.

Guo, Z., Yu, F., Lin, P., Wise, S., and Lowengrub, J., "A diffuse domain method for two-phase flows with large density ratio in complex geometries," J. Fluid Mech. **907**, A38 (2021).

Herrmann, M., "A balanced force refined level set grid method for two-phase flows on unstructured flow solver grids," J. Comput. Phys. **227**, 2674–2706 (2008).

Hu, Y., Li, D., and Niu, X., "Phase-field-based lattice Boltzmann model for multiphase ferrofluid flows," Phys. Rev. E **98**, 033301 (2018).

Hu, Y., Li, D., Niu, X., and Shu, S., "A diffuse interface lattice Boltzmann model for thermocapillary flows with large density ratio and thermophysical parameters contrasts," Int. J. Heat Mass Transfer **138**, 809–824 (2019).

Hua, H., Shin, J., and Kim, J., "Level set, phase-field, and immersed boundary methods for two-phase fluid flows," J. Fluids Eng. **136**, 021301 (2014).

Jacqmin, D., "Calculation of two-phase Navier–Stokes flows using phase-field modeling," J. Comput. Phys. **155**, 96–127 (1999).

Jamet, D., and Misbah, C., "Thermodynamically consistent picture of the phase-field model of vesicles: Elimination of the surface tension," Phys. Rev. E **78**, 041903 (2008).

Jamshidi, F., Heimel, H., Hasert, M., Cai, X., Deutschmann, O., Marschall, H., and Wörner, M., "On suitability of phase-field and algebraic volume-of-fluid OpenFOAM® solvers for gas–liquid microfluidic applications," Comput. Phys. Commun. **236**, 72–85 (2019).

Jeong, D., and Kim, J., "Conservative Allen–Cahn–Navier–Stokes system for incompressible two-phase fluid flows," Comput. Fluids **156**, 239–246 (2017).

Joshi, V., and Jaiman, R. K., "A positivity preserving and conservative variational scheme for phase-field modeling of two-phase flows," J. Comput. Phys. **360**, 137–166 (2018).

Khatavkar, V. V., Anderson, P. D., Duineveld, P. C., and Meijer, H. E. H., "Diffuse-interface modelling of droplet impact," J. Fluid Mech. **581**, 97 (2007).

Kim, J., "A continuous surface tension force formulation for diffuse-interface models," J. Comput. Phys. **204**, 784–804 (2005).

Kim, J., "Phase-field models for multi-component fluid flows," Commun. Comput. Phys. **12**, 613–661 (2012).

Kim, J., and Kang, K., "A numerical method for the ternary Cahn–Hilliard system with a degenerate mobility," Appl. Numer. Math. **59**, 1029–1042 (2009).

Kim, J., Lee, S., and Choi, Y., "A conservative Allen–Cahn equation with a space–time dependent Lagrange multiplier," Int. J. Eng. Sci. **84**, 11–17 (2014).

Leal, L. G., "Advanced transport phenomena: Fluid mechanics and convective transport processes," in *Cambridge Series in Chemical Engineering* (Cambridge University Press, 2010).

Lee, A. A., Münch, A., and Suli, E., "Sharp-interface limits of the Cahn–Hilliard equation with degenerate mobility," SIAM J. Appl. Math. **76**, 433–456 (2016).

Lee, D., and Kim, J., "Comparison study of the conservative Allen–Cahn and the Cahn–Hilliard equations," Math. Comput. Simul. **119**, 35–56 (2016).

Lee, D., and Kim, Y., "Novel mass-conserving Allen–Cahn equation for the boundedness of an order parameter," Communications Nonlinear Sci. Numer. Simul. **85**, 105224 (2020).

Li, Q. Z., Lu, Z. L., Zhou, D., Niu, X. D., Guo, T. Q., and Du, B. C., "Unified simplified multiphase lattice Boltzmann method for ferrofluid flows and its application," Phys. Fluids **32**, 093302 (2020).
Li, Y., Choi, J. I., and Kim, J., "A phase-field fluid modeling and computation with interfacial profile correction term," Commun. Nonlinear Sci. Numer. Simul. **30**, 84–100 (2016).
Liang, H., Xu, J., Chen, J., Wang, H., Chai, Z., and Shi, B., "Phase-field-based lattice Boltzmann modeling of large-density-ratio two-phase flows," Phys. Rev. E **97**, 033309 (2018).
Liu, C., "On the convective Cahn–Hilliard equation with degenerate mobility," J. Math. Anal. Appl. **344**, 124–144 (2008).
Liu, C., and Shen, J., "A phase field model for the mixture of two incompressible fluids and its approximation by a Fourier-spectral method," Phys. D **179**, 211–228 (2003).
Liu, X., Ji, Y., Deng, Y., and Wu, Y., "Advection of droplet collision in centrifugal microfluidics," Phys. Fluids **31**, 032003 (2019).
Ma, C., Wu, J., and Zhang, T., "A high order spectral difference-based phase field lattice Boltzmann method for incompressible two-phase flows," Phys. Fluids **32**, 122113 (2020).
Maffettone, P., and Minale, M., "Equation of change for ellipsoidal drops in viscous flow," J. Non-Newtonian Fluid Mech. **78**, 227–241 (1998).
Magaletti, F., Picano, F., Chinappi, M., Marino, L., and Casciola, C. M., "The sharp-interface limit of the Cahn–Hilliard/Navier–Stokes model for binary fluids," J. Fluid Mech. **714**, 95 (2013).
Magnini, M., Pulvirenti, B., and Thome, J., "Characterization of the velocity fields generated by flow initialization in the CFD simulation of multiphase flows," Appl. Math. Modell. **40**, 6811–6830 (2016).
Mirjalili, S., Ivey, C. B., and Mani, A., "A conservative diffuse interface method for two-phase flows with provable boundedness properties," J. Comput. Phys. **401**, 109006 (2020).
Niethammer, B. S., "Existence and uniqueness of radially symmetric stationary points within the gradient theory of phase transitions," Eur. J. Appl. Math. **6**, 45–67 (1995).
Niu, X. D., Li, Y., Ma, Y. R., Chen, M. F., Li, X., and Li, Q. Z., "A mass-conserving multiphase lattice Boltzmann model for simulation of multiphase flows," Phys. Fluids **30**, 013302 (2018).
Plapp, M., "Multiphase microfluidics: The diffuse interface model," in *Phase-Field Models*, Volume 538 of CISM Courses and Lectures, edited by Mauri, R. (Springer, Vienna, 2012), pp. 129–175.
Rettenmaier, D., Deising, D., Ouedraogo, Y., Gjonaj, E., De Gersem, H., Bothe, D., Tropea, C., and Marschall, H., "Load balanced 2D and 3D adaptive mesh refinement in OpenFOAM," SoftwareX **10**, 100317 (2019).
Rubinstein, J., and Sternberg, P., "Nonlocal reaction-diffusion equations and nucleation," IMA J. Appl. Math. **48**, 249–264 (1992).
Shah, A., Sabir, M., and Ayub, S., "An adaptive time-stepping scheme for the numerical simulation of Cahn–Hilliard equation with variable mobility," ZAMM-J. Appl. Math. Mech. **99**, e201800246 (2019).
Shapira, M., and Haber, S., "Low Reynolds number motion of a droplet in shear flow including wall effects," Int. J. Multiphase Flow **16**, 305–321 (1990).
Sibley, D. N., Nold, A., and Kalliadasis, S., "Unifying binary fluid diffuse-interface models in the sharp-interface limit," J. Fluid Mech. **736**, 5–43 (2013).
Soligo, G., Roccon, A., and Soldati, A., "Mass-conservation-improved phase field methods for turbulent multiphase flow simulation," Acta Mech. **230**, 683–696 (2019).
Sun, Y., and Beckermann, C., "Sharp interface tracking using the phase-field equation," J. Comput. Phys. **220**, 626–653 (2007).
Taylor, G. I., "The formation of emulsions in definable fields of flow," Proc. R. Soc. London, Ser. A **146**, 501–523 (1934).
Tryggvason, G., Bunner, B., Esmaeeli, A., Juric, D., Al-Rawahi, N., Tauber, W., Han, J., Nas, S., and Jan, Y. J., "A front-tracking method for the computations of multiphase flow," J. Comput. Phys. **169**, 708–759 (2001).
Vachaparambil, K. J., and Einarsrud, K. E., "Comparison of surface tension models for the volume of fluid method," Processes **7**, 542 (2019).
Vananroye, A., Van Puyvelde, P., and Moldenaers, P., "Effect of confinement on the steady-state behavior of single droplets during shear flow," J. Rheol. **51**, 139–153 (2007).
Vasilopoulos, Y., "An alternative phase-field interfacial tension force representation for binary fluid systems," Phys. Fluids **32**, 102101 (2020).
Wacławczyk, T., "On a relation between the volume of fluid, level-set and phase field interface models," Int. J. Multiphase Flow **97**, 60–77 (2017).
Wang, Y., Shu, C., Yang, L., and Yuan, H., "On the re-initialization of fluid interfaces in diffuse interface method," Comput. Fluids **166**, 209–217 (2018).
Wazwaz, A. M., Rach, R., and Duan, J. S., "Adomian decomposition method for solving the Volterra integral form of the Lane–Emden equations with initial values and boundary conditions," Appl. Math. Comput. **219**, 5004–5019 (2013).
Wörner, M., "Numerical modeling of multiphase flows in microfluidics and micro process engineering: A review of methods and applications," Microfluid. Nanofluid. **12**, 841–886 (2012).
Wörner, M., Samkhaniani, N., Cai, X., Wu, Y., Majumdar, A., Marschall, H., Frohnapfel, B., and Deutschmann, O., "Spreading and rebound dynamics of sub-millimetre urea-water-solution droplets impinging on substrates of varying wettability," Appl. Math. Modell. **95**, 53–73 (2021).
Yang, X., Feng, J. J., Liu, C., and Shen, J., "Numerical simulations of jet pinching-off and drop formation using an energetic variational phase-field method," J. Comput. Phys. **218**, 417–428 (2006).
Yeoh, G. H., and Tu, J., *Computational Techniques for Multiphase Flows* (Butterworth-Heinemann, 2010).
Yuan, H., Chen, Z., Shu, C., Wang, Y., Niu, X., and Shu, S., "A free energy-based surface tension force model for simulation of multiphase flows by level-set method," J. Comput. Phys. **345**, 404–426 (2017).
Yue, P., "Thermodynamically consistent phase-field modelling of contact angle hysteresis," J. Fluid Mech. **899**, A15 (2020).
Yue, P., Feng, J. J., Liu, C., and Shen, J., "A diffuse-interface method for simulating two-phase flows of complex fluids," J. Fluid Mech. **515**, 293 (2004).
Yue, P., Zhou, C., and Feng, J. J., "Spontaneous shrinkage of drops and mass conservation in phase-field simulations," J. Comput. Phys. **223**, 1–9 (2007).
Zanella, R., Tegze, G., Le Tellier, R., and Henry, H., "Two-and three-dimensional simulations of Rayleigh–Taylor instabilities using a coupled Cahn–Hilliard/Navier–Stokes model," Phys. Fluids **32**, 124115 (2020).
Zhai, S., Weng, Z., and Feng, X., "Investigations on several numerical methods for the non-local Allen–Cahn equation," Int. J. Heat Mass Transfer **87**, 111–118 (2015).
Zhang, Q., Qian, T. Z., and Wang, X. P., "Phase field simulation of a droplet impacting a solid surface," Phys. Fluids **28**, 022103 (2016).
Zhang, T., Wu, J., and Lin, X., "An interface-compressed diffuse interface method and its application for multiphase flows," Phys. Fluids **31**, 122102 (2019).
Zhang, Z., and Tang, H., "An adaptive phase field method for the mixture of two incompressible fluids," Comput. Fluids **36**, 1307–1318 (2007).
Zhu, G., Kou, J., Yao, B., Wu, Y. S., Yao, J., and Sun, S., "Thermodynamically consistent modelling of two-phase flows with moving contact line and soluble surfactants," J. Fluid Mech. **879**, 1 (2019).
Zu, Y., and He, S., "Phase-field-based lattice Boltzmann model for incompressible binary fluid systems with density and viscosity contrasts," Phys. Rev. E **87**, 043301 (2013).